**AWARD NUMBER:**

W81XWH-15-1-0147

**TITLE:**

Virtual Tissue Modeling for Realtime Surgical and Inverventional Procedure Simulation

**PRINCIPAL INVESTIGATOR:**

Peyman Benharash, M.D.

**CONTRACTING ORGANIZATION:** **University of California, Los Angeles**
Los Angeles, CA 90095

**REPORT DATE: July 2017**

**TYPE OF REPORT: Annual**

**PREPARED FOR:**

U.S. Army Medical Research and Materiel Command

Fort Detrick, Maryland 21702-5012

**DISTRIBUTION STATEMENT:**

# REPORT DOCUMENTATION PAGE

*Form Approved*
*OMB No. 0704-0188*



| 1. REPORT DATE | 2. REPORT TYPE | 3. DATES COVERED |
|---|---|---|
| July 2017 | Annual | 1 Jul 2016- 30 Jun 2017 |

**4. TITLE AND SUBTITLE**

Virtual Tissue Modeling for Realtime Surgical and Inverventional Procedure Simulation

**5a. CONTRACT NUMBER**

**5b. GRANT NUMBER**
W81XWH-15-1-0147

**5c. PROGRAM ELEMENT NUMBER**

**6. AUTHOR(S)**

Peyman Benharash, M.D.

E-Mail: benharash@gmail.com

**5d. PROJECT NUMBER**

**5e. TASK NUMBER**

**5f. WORK UNIT NUMBER**

**7. PERFORMING ORGANIZATION NAME(S) AND ADDRESS(ES)**

University of California, Los Angeles
11000 Kinross Ave, Ste 102
Los Angeles, CA 90095-2000

**8. PERFORMING ORGANIZATION REPORT NUMBER**

**9. SPONSORING / MONITORING AGENCY NAME(S) AND ADDRESS(ES)**

U.S. Army Medical Research and Materiel Command
Fort Detrick, Maryland 21702-5012

**10. SPONSOR/MONITOR'S ACRONYM(S)**

**11. SPONSOR/MONITOR'S REPORT NUMBER(S)**

**12. DISTRIBUTION / AVAILABILITY STATEMENT**

Approved for Public Release; Distribution Unlimited

**13. SUPPLEMENTARY NOTES**

**14. ABSTRACT**

This project aims to develop a platform for modeling of virtual tissues to be used in simulation of surgical and interventional procedures. The investigative team has made major advances in collection of mechanical tissue properties of the liver, integration into complex constitutive models, re-tooling the hemodynamic simulation model, and delivery of physics based visual models. Moreover, the group has been able to successfully demonstrate interaction of the virtual liver model with external forces including external shock wave and actual ballistic projectile. The results of the work performed during this award period have allowed for a physics-based model of tissue trauma and hemorrhage based on actual physical properties of the liver in a viscoeleastic model, with superimposed hemorrhage using a smooth particle hydrodynamics method, in order to generate a high fidelity virtual model of the said organ.

**15. SUBJECT TERMS**

liver constitutive modeling, material point methods, fluid/elastic multi-species continuum, hepatic tissue, hysteresis, compression, cardiovascular network simulation, hemorrhage modeling, smoothed-particle hydrodynamics

| 16. SECURITY CLASSIFICATION OF: | | | 17. LIMITATION OF ABSTRACT | 18. NUMBER OF PAGES | 19a. NAME OF RESPONSIBLE PERSON |
|---|---|---|---|---|---|
| a. REPORT | b. ABSTRACT | c. THIS PAGE | | | USAMRMC |
| Unclassified | Unclassified | Unclassified | Unclassified | 53 | 19b. TELEPHONE NUMBER *(include area code)* |

# Table of Contents

**INTRODUCTION**:

The UCLA Center for Advanced Surgical and Interventional Technology (CASIT) shall lead a 3-year R&D program, "Virtual Tissue Modeling for Real-time Surgical and Interventional Procedure Simulation," to develop and evaluate a new virtual tissue modeling methodology for use in military medical training simulators for forward surgical and interventional care of combat injuries.

**KEYWORDS**:

liver constitutive modeling, material point methods, fluid/elastic multi-species continuum, hepatic tissue, hysteresis, compression, cardiovascular network simulation, hemorrhage modeling, smoothed-particle hydrodynamics

**ACCOMPLISHMENTS**:

- **What were the major goals of the project?**

The overall project goals are to develop a general framework for creation and sharing of virtual tissue models; create a prototype virtual tissue simulation of the liver and associated soft tissue and fluidic physiological systems; develop and integrate needed mathematical models, constitutive models, and interactive graphical models as a functional system of physics-based dynamic tissue simulations capable of real-time interaction appropriate for medical training simulators. The constitutive models shall be populated with validated physiological material properties. Virtual injury mechanisms and surgical tools shall be created for manipulation of the virtual tissue and methods developed for integrating component models (e.g. the liver) into a virtual patient body habitus model. Results shall be documented in a final report. The system shall be demonstrated in either a video or online interactive presentation format. The technologies and capabilities that shall be included are: computational simulation, graphical simulation, constitutive models, material property data acquisition, toolkits for injury and surgical procedures, and an online model repository and sharing system.

The goals for Y2 were to continue research and development in the following focal areas:

1. Fluid dynamics & tissue constitutive modeling
2. Numerical methods for real-time modeling
3. Biomechanical and graphical modeling of organs
4. Tissue properties measurement and validation
5. Body habitus graphical and physical modeling
6. Medical requirements and assessment
7. Open standards development for virtual anatomic models
8. Project advisory activity
    a) Formation of advisory panel of military medicine SMEs
    b) Formation of advisory panel of surgical and interventional simulation industry SMEs

- **What was accomplished under these goals?**

1. Fluid dynamics & tissue constitutive modeling

There are two overall objectives of the fluid dynamics modeling team in this project. The first objective is to develop a comprehensive network model of the human cardiovascular system, with associated cardiac and autoregulation sub models, coupled with a fluid and nutrient transport model of the liver. The second major objective is to create a computational fluid dynamics simulation, based on smoothed particle hydrodynamics (SPH), of visualized bleeding from injury or surgical sites in the virtual model of the liver. These objectives are intertwined, since the visualized bleeding simulator requires the dynamic inflow conditions from the network model.

During Q1 of Y2, we continued our development on three target areas that will comprise the fluid dynamics and elasticity components of the virtual tissue model.

The first target area involves the development of a modular real-time network model of the human cardiovascular system. This model, which provides local pressure and flow rate in the vascular tree, will drive the local network model of the organ (liver). We have now combined the various component submodels — systemic vasculature, cardiac, and autoregulation — into a single Matlab-based model, and demonstrated its performance on a basic hemorrhage event. The vascular submodel is expressed in the frequency domain, while the other submodels are in the time domain.

The second target area involves the extension of our bleeding visualization framework to the liver. During Q1 of Y2, we have performed a visualization of hemorrhage during a ballistic penetration of the liver. This is the first time in which we have coupled the bleeding simulation to the deforming liver geometry, so it's an important milestone. We are currently pursuing a longer-duration simulation of a similar injury event.

We have also been exploring the equations of poro-elasticity, which govern the mechanics of a porous, elastic, fluid-filled material, such as the perfused liver. These equations will form the basis for the ultimate form of our virtual liver modeling, since they will account for the effect of blood (and bile) on the liver deformation, and also provide a clear coupling between the elastic deformation and the bleeding simulations. In this quarter, we have established the governing equations and proposed a candidate hyperelastic constitutive model for liver tissue.

During Q2 of Y2, we continued our development on three target areas that will comprise the fluid dynamics and elasticity components of the virtual tissue model.

The first target area involves the extension of our bleeding visualization framework to the liver. During this quarter, we carried out a more refined and longer-duration simulation of a ballistic penetration of the liver. We are currently pursuing a second simulation involving a complete resection of the liver. These simulations have been very promising, and have been helpful for refining our procedures for introducing computational blood particles into the scenario. For example, we now are able to determine which major vascular segments in the three major networks (portal vein, hepatic artery, hepatic vein) within the liver have been severed by a given injury, and introduce bleeding from these precise locations.

However, the simulation still relies on a few ad hoc aspects: one, we are only guessing at the pressure and flow rate of the severed vessels; and two, we carry out the simulation as a one-way coupling: tissue

deformation and failure is simulated first, and these are used a posteriori to simulate bleeding in a geometry of prescribed deformation. Both of these aspects are currently being addressed.

In order to obtain pressure and flow rate at the site of the injury (or treatment), we have been developing a modular real-time autoregulated network model of the cardiovascular system and a local network model of the liver. In the previous quarter, we recognized some drawbacks of our previous submodel of the systemic vasculature, which had been expressed in the frequency domain. During this quarter, we have been developing a time-domain version of the submodel, which enables more consistency and flexibility when connecting it to the cardiac and autoregulatory submodels. This work should be completed by the end of the next quarter.

In order to more strongly couple the dynamics of the bleeding and the tissue deformation, we have been developing the equations of poro-elasticity, which govern the mechanics of a porous, elastic, fluid-filled material, such as the perfused liver. These equations will form the basis for the ultimate form of our virtual liver modeling, since they will account for the effect of blood (and bile) on the liver deformation, and also provide a clear coupling between the elastic deformation and the bleeding simulations. In this quarter, we have been carrying out some preliminary simulations of poro-elasticity in simple scenarios, such as a wet sponge under compression.

During Q3 of Y2, we continued our development on three target areas that will comprise the fluid dynamics and elasticity components of the virtual tissue model.

In the first target area, we applied our bleeding visualization framework to a complete resection of the liver. This virtual resection exposed a number of severed vascular segments in the associated network model of the liver vasculature. Computational blood particles were introduced at the distal ends of these segments and allowed to flow, using approximate flow rates based on the flow into the hepatic artery. This was mostly carried out to develop more guidance on how much resolution is needed to achieve a good rendering of the bleeding. The movie is embedded below:

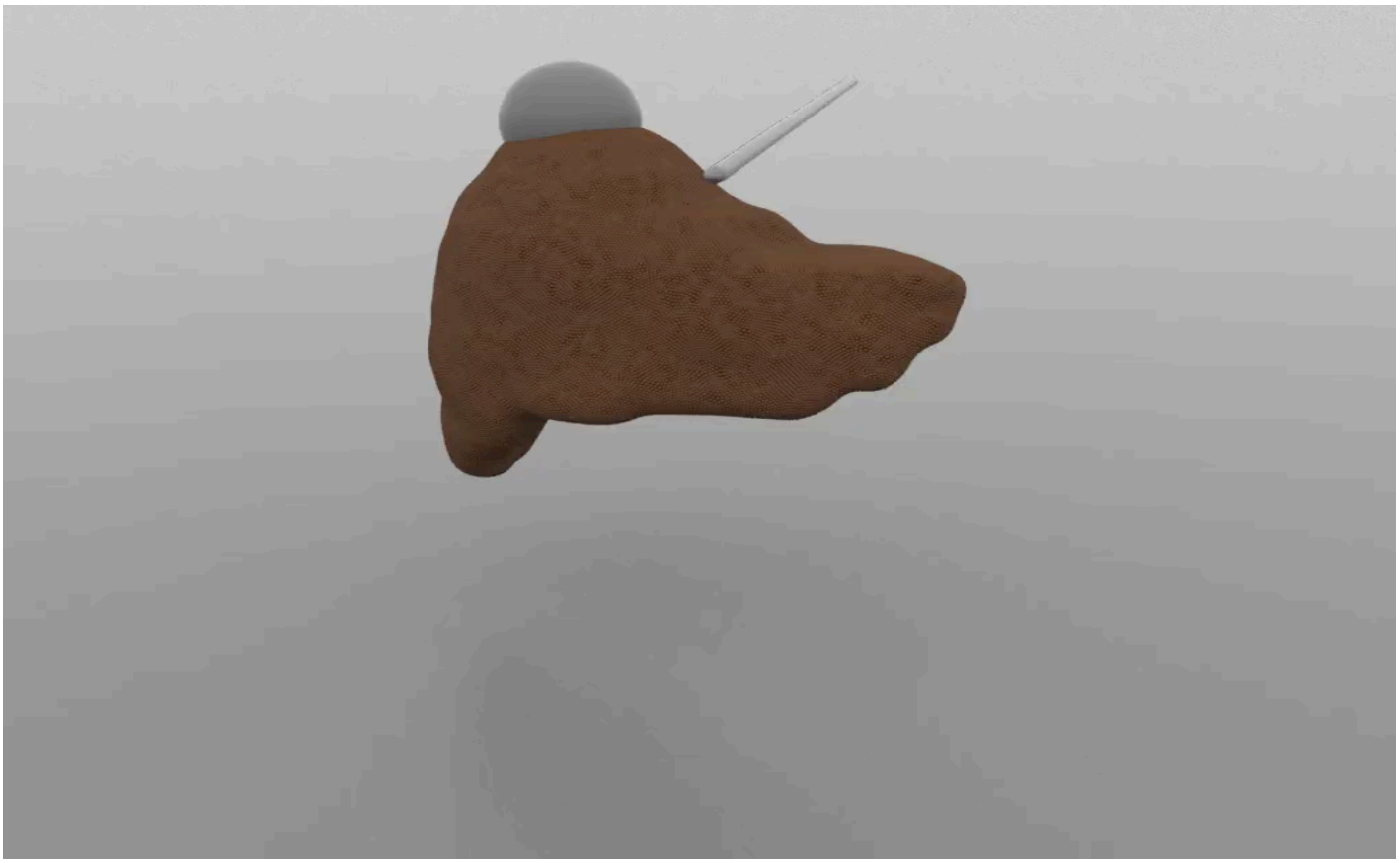

As mentioned in the previous report, the simulation still relies on a few ad hoc aspects: one, we are only guessing at the pressure and flow rate of the severed vessels; and two, we carry out the simulation as a one-way coupling: tissue deformation and failure is simulated first, and these are used a posteriori to simulate bleeding in a geometry of prescribed deformation. Both of these aspects are currently being addressed, as we describe below.

In order to obtain pressure and flow rate at the site of the injury (or treatment), we have been developing a modular real-time autoregulated network model of the cardiovascular system and a local network model of the liver. During this quarter, we mostly completed our time-domain version of the 1-d vascular submodel, and this is closed with the cardiac and neurogenic regulatory submodels. The code was originally written in Matlab, a non-compiled language that isn't very efficient, so we will rewriting this in Julia, a very good and modular language that exhibits much better performance. We will also be testing the full cardiovascular model with reported results in the literature.

In order to more strongly couple the dynamics of the bleeding and the tissue deformation, we have been developing the equations of poro-elasticity, which govern the mechanics of a porous, elastic, fluid-filled material, such as the perfused liver. In this quarter, we implemented the governing "bi-phasic" equations for this model, using Smoothed Particle Hydrodynamics (SPH), the same methodology that we had previously used for just the blood phase in our uncoupled visualizations. Here, we have used SPH for the solid phase, as well. This SPH bi-phasic simulation tool is completely novel. We have begun carrying out simulations of simple configurations of a spongy cubic specimen: compression (with associated ejection of the liquid phase) and expansion (the absorption of liquid from a bath in which the specimen is immersed). These have allowed us to tune some of the numerical parameters.

During Q4 of Y2, we focused on the continuing development of the two target areas that will comprise the fluid dynamics and elasticity components of the virtual tissue model: a simulation tool for the coupled fluid-tissue mechanics of liver and its constituent liquids, driven by an auto-regulated model of the full cardiovascular system. We also completed our efforts on our "uncoupled" bleeding visualizations, since these will be supplanted by the coupled fluid-tissue simulations.

The overall objective of this simulation framework is to enable a physics-driven, visually faithful rendering of the liver, when subjected to various injuries or surgical interventions. This requires

- A simulation of the liver tissue mechanics, with material properties obtained by mechanical testing of liver samples, coupled with
- A simulation of the spatially resolved flow of the homogeneous interstitial blood (and bile) phase in the perfused tissue
- A complete set of dynamically-variable "inflow" and "outflow" conditions for the liver, from the systemic vasculature and cardiac function, and the feedback control provided by the autonomic response to, e.g. hemorrhage or pharmacological intervention.

We have pursued the first two of these in a fully coupled manner, through a bi-phasic computational model, in which the solid (tissue) and liquid (blood and bile) are regarded as superimposed phases, which interact through relative drag force and a constraint that preserves their total volume fraction. This model accounts for essential physical behaviors: tissue swelling by absorption of liquid, expulsion of liquid by local compression, and overall mechanical response of the perfused tissue under various loadings. Beginning with the previous quarter, and continuing in this quarter, we have computationally implemented these equations with Smoothed Particle Hydrodynamics (SPH). We have been testing and refining this implementation using simple scenarios that allow us to identify and fix problems that would also be present in the full liver simulation. Among these simple problems are the mechanical tests pursued by the Candler research group on this team.

In parallel with this, we have also been addressing the other component, the cardiovascular model. We have developed and implemented (in a language called Julia) a modular real-time autoregulated network model of the cardiovascular system. During this quarter, we have been evaluating this computational model against reported results in the literature, such as the pulsatile waveform generated at the ascending aorta under normal physiological conditions, the evolution of the pressure and flow rate signals into the major peripheral arteries, and the behaviors of the heart rate, systemic vascular resistance, and other gross physiological parameters in response to disruptions that trigger the sympathetic and parasympathetic nervous system. One of these triggers will, of course, be hemorrhage in the liver, so we place a premium on getting this response correct.

2. Numerical methods for real-time modeling

During Q1 of Y2, we further developed the constitutive model of the liver including the effects of blood as a porous multi-species medium. We will soon enter into a fitting stage where we directly fit experimental observation with our model.

We additionally included the effects of damage/topological change of the vascular during traumatic injury simulation. We have further developed an excision tool to allow for simulated surgical manipulation, e.g. in response to the traumatic injuries we have simulated.

We now have a model that consists of an elastic surface membrane, a hyperelastic bulk interior, an embedded elastic vascular as well as a porous fluid matrix. Furthermore, this model can be simulated with considerable flexibility to topological change and extreme deformation.

During Q2 of Y2, we completed an investigation of coupling terms between the porous fluid matrix and the bulk fluid interior of the liver. We use a multi-species continuum approach to do this. Blood is modeled as its own continuum species and the elastic fluid matrix as another. The two materials individually obey conservation of mass and momentum. The mass density and momentum of the fluid/matrix model is the sum of the individual species mass density and momentum. This defines the velocity of the combined phases as the mass average velocities of the species and balance of linear momentum follows if we define the effective fluid/matrix stress as the sum of the individual species stresses. The individual species momenta evolve under the influence of their local stress, as well as a momentum exchange term between the species. This term is stiff and we have developed appropriate implicit time stepping treatments of the term. This is done via the material point method (MPM). Our initial investigations have included the effect of the vascular structure in the elasticity and we have demonstrated our method on oozing and bleeding following liver surgical incision. We have also begun the model fitting phase for with a suite of experiments that can be used to fit the model to data.

During Q3 of Y2, we have continued the process of fitting our model to experimental data. We designed and started the development of surgically relevant simulation examples involving sutures incisions in soft tissues. We explored various algorithmic options for this.

This quarter we completed an investigation of coupling terms between the porous fluid matrix and the bulk fluid interior of the liver. We use a multi-species continuum approach to do this. Blood is modeled as its own continuum species and the elastic fluid matrix as another. The two materials individually obey conservation of mass and momentum. The mass density and momentum of the fluid/matrix model is the sum of the individual species mass density and momentum. This defines the velocity of the combined phases as the mass average velocities of the species and balance of linear momentum follows if we define the effective fluid/matrix stress as the sum of the individual species stresses. The individual species momenta evolve under the influence of their local stress, as well as a momentum exchange term between the species. This term is stiff and we have developed appropriate implicit time stepping treatments of the term. This is done via the material point method (MPM). Our initial investigations have included the effect of the vascular structure in the elasticity and we have demonstrated our method on oozing and bleeding following liver surgical incision. We have also begun the model fitting phase for with a suite of experiments that can be used to fit the model to data.

During Q4 of Y2, we have continued the process of developing new techniques for cutting soft tissues in Material Point Method simulations. Furthermore, we have developed a framework for generating libraries of simulation data that will serve as the enabling technology for real-time computing applications. We hope to achieve real-time technology by leveraging advances in machine learning and we are investigating how this can be done in the context of soft tissue simulation.

3. Biomechanical and graphical modeling of organs

During Q1 of Y2, the overall goal is to develop a liver elastography framework using 4DCT and 4D MR based imaging paradigm coupled with the hyperelastic liver tissue modeling. For this quarter, we intend to develop an in-house codebase that will enable doing the same.

**Model guided liver elastography framework:** The focus of our research is to formulate a method to perform high-precision image-based liver elastography using patient-specific 4DCT data acquired during radiotherapy treatment planning, and to systematically validate and quantify the accuracy of this methodology. A linear elastic biomechanical model, which has been previously used for representing head and neck (Neylon, Qi et al. 2015) and breast (Hasse, Neylon et al. 2016) deformations, will be employed as a deformation model to represent the lung anatomy. Each mass element of the biomechanical simulation represents a corresponding voxel of tissue from the source image of the 4DCT data. Lung surface displacements were applied as boundary constraints for the model-guided liver tissue elastography, while the inner voxels were allowed to deform according to the linear elastic forces within the model. A novel biomechanically-based anisotropic convergence magnification technique was applied to the inner voxel in order to amplify the subtleties of the interior deformation. The inverse elasticity problem is solved by implementing a gradient-based search algorithm.

**Background:** Elastography is a non-invasive way to image the local elastic properties of soft tissue. Liver elastography has many clinical benefits, including the ability to discriminate between healthy and diseased tissue, visualize liver tissue changes during a clinical intervention, and detect pathological changes within the liver. Current elastography techniques involve applying low frequency oscillation to tissue and measuring the resulting deformation with US, extracting elasticity from the observed motion. Another technique, magnetic resonance elastography (MRE), uses synchronized cyclic shear wave displacement, encoded into the phase of the MR signal, to derive the elastic properties of tissue. Despite the usefulness of image-based elastography and its proven diagnostic accuracy in the thyroid, breast, and prostate, it has not yet been thoroughly investigated in the liver, particularly within the modeling and simulation context, where the usage of multiple imaging modalities also raises the need to precisely register the multi-modal data, a problem has not been fully addressed so far.

**In-house codebase development**: As part of the grant, we have instantiated a liver elastography approach which will enable the liver tissue elasticity to be estimated using conventional 4D imaging that is typically employed for deformable organs such as the lung. Conventional approach using MATLAB based solvers that typically employ a CPU based computing environment will not be able to address the computational complexity. Using a GPU based framework developed ground-up enables us to perform the elastography within 1 hour of computing time.

**Iterative hyperelastic value determination:** To move from the initial estimates developed in §C.2.2.3 to the final estimates, we will employ forward model-guided elastography, where the forward model (Finite Element) will be employed to generate deformations using the previously estimated hyperelastic properties. The hyperelasticity will be iteratively optimized until a preset convergence is achieved. During the deformation phase, the outer lung surfaces will be constrained based on their deformable image registration displacements (SA1) while the inner lung voxels will be allowed to deform using their transient hyperelasticity. At steady state deformation, a unidirectional perturbation force will be applied to the inner voxels in order to amplify their convergence. The optimization of the estimated hyperelastic values will be performed using gradient descent and fast simulated annealing, which are well suited for hyperelasticity estimations. The desired hyperelastic properties *R* will be determined using the relation,

$$R = argmin\|D - R \otimes F\| + B\sqrt{|\nabla f^2|} + \varepsilon \qquad (1)$$

where *D* represents the lung deformation (SA1), *F* the applied force, and *B* is a regularization parameter. The deformation operator will consist of the eigenvalues of the 2nd Piola-Kirchoff stress tensor's inverse. In vector form, *D* is expressed as a convolution of *F* and *R* (Equation 4).

Because the hyperelasticity is numerically described as a sequence of parameters, optimizing the hyperelasticity is a multi-local minima problem. To address this issue, a fast-simulated annealing algorithm will be used to optimize the hyperelasticity simultaneous to a regularization, similarly to our previously published application in the breast.

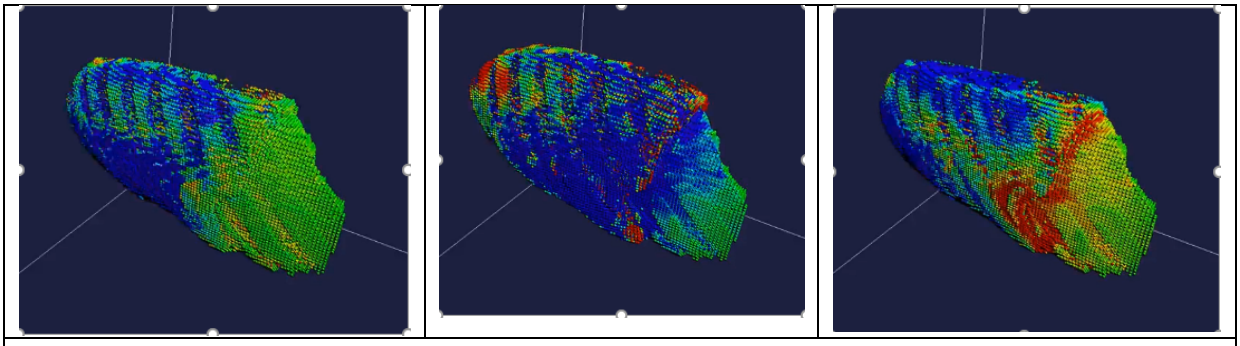

Fig 1. Lung and liver model setup for elasticity estimation. Fig a shows the start of lung inhalation (tightening colored in blue). (b) shows the end of the inhalation where the liver constriction is caused by the expansion fo the lung. (c) shows the end of exhalation where the liver expansion is caused by the contraction of the overall lung.

**Deformation setup**: A physics-based biomechanical model of the lung and liver was used as a forward model to solve the inverse elasticity problem. The forward model focused on iteratively computing the liver tissue deformation for a given lung surface displacement for a given liver elasticity distribution. Fig 1 shows the deformation interaction between the lung and liver. For our research, we consider the lung models as the boundary constraint for the liver elastography estimation.

**Preliminary results using synthetic lung phantoms:** We published a systematic analysis of a linear version of the elasticity estimation process using synthetic lung phantoms, normal and emphysemic lung, with and without embedded lung tumors, enabling us to test the algorithms using ground-truth tissue elasticity and lung deformations. Fig 2 presents the results. Employing 18 synthetic lung phantoms, our results showed that 99.98% (right lung) and 99.92% (left lung) of the voxels converged with an average of within 0.5 mm of the ground-truth displacement values, which resulted in 91.59% (right lung) and 91.87% (left lung) of the voxels converging within 1 kPa of the ground-truth elasticity. Figure 4 shows the linear elasticity estimate for a normal lung. Figure 4b shows the estimation errors were less than ~0.8 KPa. While these results employed linear elasticity, they indicate feasibility of the more general hyperelastic approach. The simulations of emphysemic lung and lung tumors also showed good agreement with the estimated and ground truth elasticity. Emphysema lowers the elastic modulus of normal tissue, and malignant tumors generally have a greater elasticity than surrounding tissue. On average, the methodology converged with displacement accuracy values of 99.95%, 99.94%, and 99.95% for simulated emphysematous, cancerous, and normal tissues respectively, corresponding to 91.90%, 91.68%, and 91.62% of voxels converging within 1 kPa of the ground-truth elasticity values.

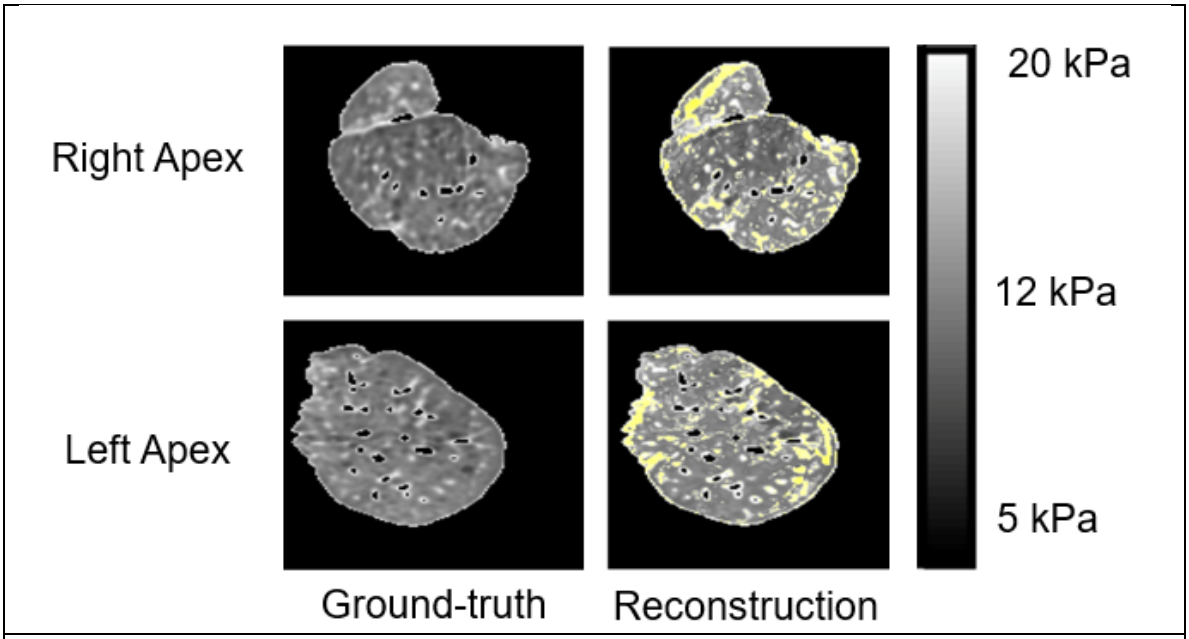


**Fig 2: A systematic assessment of model-guide elastography, when applied to lung.**

During Q2 of Y2, we studied our preliminary results using human patient data.

**Preliminary results using human patient data:** We estimated the linear elasticity for human patient datasets using the methodology discussed above. We employed both non-COPD and COPD patient lung datasets for our study. Figure 1 shows the elasticity estimation results for a non-COPD patient. The elasticity estimated from the lung deformation (figure 1a) is shown in figure 1b. Figure 2 shows the elasticity estimation results for two severe COPD lung patients. The elasticity estimated from the lung deformations (figures 2a and 2c) are shown in figures 2b and 2d. Much of these lungs have elasticity (0-2 KPa) consistent with COPD lung tissues. The difference between COPD and normal lung tissues are clear in these examples and are consistent with expected values. We conducted the elastography estimation on 13 lung cancer patients, 7 of which had COPD and the remaining had otherwise normal lungs, using images reconstructed at peak inhalation and exhalation using the techniques of Low et al [47]. These datasets simulate breath-hold at these breathing phases, avoiding the added complexity of dynamic breathing, which will be modeled in SA3. Figure 7 shows the average elasticity for voxels with HU values of -600 to -800, representing parenchymal tissues, for the 13 patients, ranked in order of average elasticity. As expected, the mean elasticity values of the COPD patients were consistently lower than the non-COPD patients. These data indicate that we are able to differentiate between COPD and non-COPD patients. We anticipate that by directly utilizing the FHFBCT images and employing hyperelastic property estimation, we will be able to provide data that investigators will be able to use to make subtler differentiations, such as those needed to evaluate treatment efficacy.

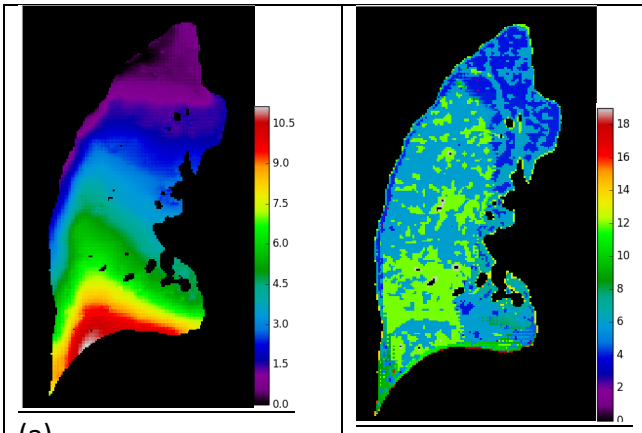


(a) (b)

**Fig 1**. 2D slice view of the deformation magnitude (in mm) for a non-COPD lung (a) is shown. The corresponding 2D slice view of the estimated elasticity (in KPa) is shown in (b).

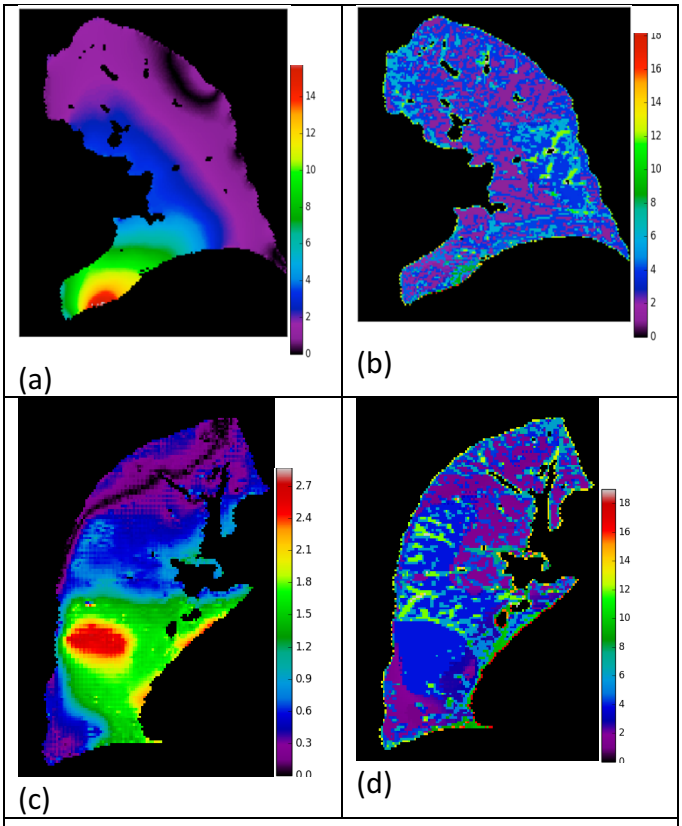


(a) (b) (c) (d)

**Fig 2**. 2D slice view of the deformation magnitude (in mm) for two COPD lung patients is shown in (a) and (c). The corresponding 2D slice view of the elasticity (in KPa) is shown in (b) and (d).

**Elastography validation techniques:** We will validate the elastography techniques using the technique by Low et al [47] to model human breathing motion. This technique uses free-breathing CT scans and a breathing motion model to create CT datasets at any breathing phase. Because SA2 involves only biomechanical property estimation and not airflow dynamics, we will create breath-hold CT scans for validating SA2. FHFBCT scans will be employed to test the full FSI model.

(a) The elasticity estimates will be validated by employing them to predict the tissue deformations and comparing the predicted deformations to the actual deformations of the breath-hold CT scans using techniques we have described when validating elasticity estimates of the head and neck and breast. We conducted this analysis with the patient data shown in Figures 5 and 6, and our observations showed that for both datasets, 95% of the voxels demonstrated <10% displacement error.

(b) We will determine if the linear elastic components of our estimated tissue elasticity values agree with published data.

(c) Elasticity properties are independent of the breathing state, and so should be our estimated properties. We will systematically exclude one or more lung geometries at specific breathing phases and re-compute the elastic properties. The property values should be the same regardless of which breathing phases are excluded; variations will indicate errors in our approach.

The primary outcome will be a voxel-by-voxel description of tissue hyperelasticity. To date, such subject-specific hyperelastic properties have not been available and will be the key contribution of the proposed work.

During Q3 of Y2, we present a novel methodology for performing lung elastography within the radiotherapy context. Our approach employed a physics-based model and a novel convergence magnification approach to estimate the lung elasticity distribution. For a systematic analysis, we employed a physics-based virtual lung phantom with CT source geometry and a heterogeneous voxel-to-voxel elasticity distribution. A set of 18 synthetic CT image datasets with known ground-truth elasticity representing normal, emphysematous, and tumor tissue within the lungs was generated and used as input for the lung elastography. During the lung elastography, we start by re-estimating the lung deformations using a deformable image registration procedure. For known phantom geometry, boundary conditions and lung deformation, we solve for the elasticity distribution by iteratively optimizing the tissue elasticity and deforming the lung model for given boundary constraints. To improve the estimation accuracy, a convergence magnification approach was formulated using a physics-based process that amplified the geometrical differences between the ground-truth and the deformed geometry. Our results showed that the model-guided approach estimated the elasticity with $91.94 \pm 5.20\%$ of voxels within 0.5 mm of ground-truth displacement and 1 kPa of the ground-truth elasticity. The novel convergence technique presented in this paper improved the accuracy of the estimated elasticity from 77.05% to 91.94%. In the systematic analysis, variations in forward model, ground-truth elasticity distribution, boundary deformation, and geometry were investigated with respect to their effect on the accuracy of the elasticity estimation technique.

**Assessing the estimation accuracy for variations in the ground-truth elastic distributions:** Table 2 lists the average results for the systematic analysis performed using the locally heterogeneous convergence magnification method. The results were also broken down by experimental category; these results are further explained in sections 4.3 – 4.4 below. Three different ground-truth elasticity distributions—emphysematous, cancerous, and normal tissue—were investigated to analyze the robustness of our methodology. On average, the methodology converged with displacement accuracy values of 99.95%, 99.94%, and 99.95% for emphysematous, cancerous, and normal tissue respectively. These results, presented in table 2 above, corresponded to 91.90%, 91.68%, and 91.62% of voxels converging within 1 kPa of the ground-truth elasticity values. Figure 9 illustrates the robustness of the methodology for reproducing different ground-truth elasticity distributions. Figure 9(a) shows the conventional elasticity reconstruction, which was the same for normal, emphysematous, and cancerous ground-truth elasticity distributions. Discrepancies between the reconstruction and the normal ground-truth elastic distribution that are greater than 1 kPa are highlighted in yellow. It can be seen that initially, the reconstruction is very different from the ground-truth, with a similarity of less than 50%.

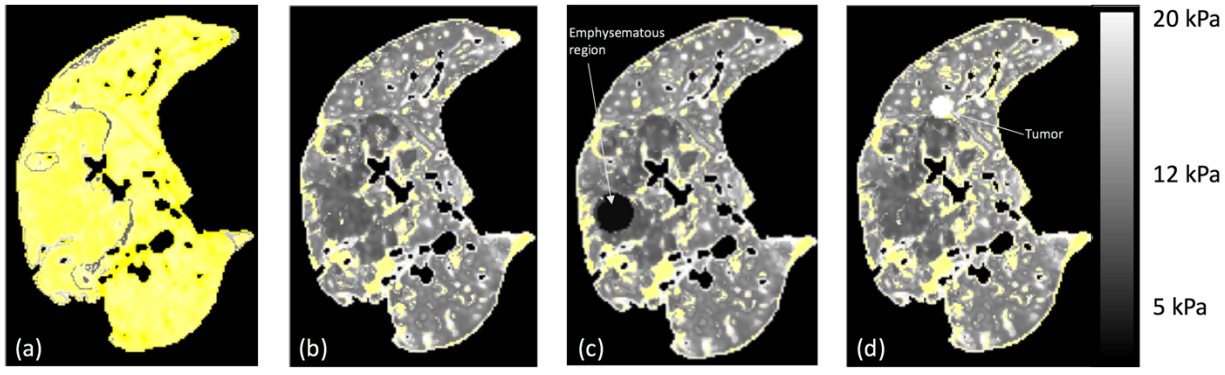


**Figure 1.** 2-D slice of middle right lung. (a) shows the conventional reconstruction for all 3 ground-truth elasticity distributions. (b) shows the novel reconstruction for normal tissue, (c) shows the reconstruction for normal tissue with emphysematous region, and (d) shows the reconstruction for normal tissue with tumor.

Discrepancies (error > 1 kPa) between the reconstructed and ground-truth distributions are highlighted in yellow.

Figure 1(b – d) show the novel elasticity reconstruction for normal, emphysematous, and cancerous tissue respectively, with the discrepancies (error > 1 kPa) between the reconstructed and ground-truth data highlighted in yellow. With similarity values of 92.73%, 93.44%, and 91.10%, it can be seen that use of the locally heterogeneous convergence magnification greatly improves the elasticity reconstruction, allowing for the visualization of emphysematous and cancerous regions within the lungs. It should be noted that for each lung geometry, cancerous and emphysematous regions were placed at different locations within the 2-D slices to ensure that the regions could be localized regardless of position. A two-sample t-test was performed between the mean values of 18 different emphysematous, 18 different cancerous, and 18 normal tissue distributions, and the observed difference was convincing enough to say that the average values of each ground-truth elasticity distribution did not differ significantly ($P > 0.05$).

**Assessing the estimation accuracy for variations in the boundary constraints:** As described in section 3.2.4 above, the outward motion of the lung boundary was constrained to three different values for each section of the lung as listed in table 1. The resulting displacement and elasticity accuracy values of the methodology are listed in table 4 below.

**Table 1.** Displacement and elasticity accuracy values for different geometries and boundary constraints.

| Lung Geometry - Boundary Constraint | Displacement Accuracy < 0.5 mm (%) | Elasticity Accuracy < 1 kPa (%) |
|---|---|---|
| **Apex – 2 mm** | 99.99 | 97.89 |
| **Apex – 4 mm** | 99.99 | 97.55 |
| **Apex – 6 mm** | 99.97 | 96.82 |
| **Middle – 3 mm** | 99.92 | 94.17 |
| **Middle – 6 mm** | 99.94 | 92.18 |
| **Middle – 9 mm** | 99.95 | 90.07 |
| **Base – 10 mm** | 99.98 | 89.37 |
| **Base – 13 mm** | 99.99 | 82.86 |
| **Base – 16 mm** | 99.78 | 84.80 |

Overall averages are listed for the three different boundary constraints in table 2 above. A two-sample t-test was performed on these values, and it was found that there were no significant differences between the results regardless of whether boundary constraint 1, 2, or 3 was used for each geometry.

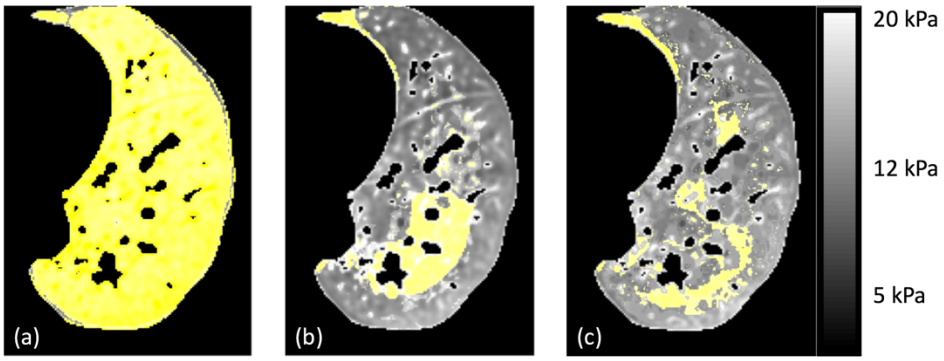

**Figure 2.** 2-D elasticity reconstruction of base of left lung. (a) shows conventional reconstruction, (b) shows novel reconstruction with 10-mm boundary constraint, and (c) shows novel reconstruction with 16-mm boundary constraint. Discrepancies (error > 1 kPa) between the reconstructed and ground-truth distributions are highlighted in yellow.

Figure 2 further illustrates that the reconstruction converges similarly regardless of the boundary constraint magnitude. Figure 10(a) shows the conventional reconstruction of the base of the left lung, (b) shows the reconstruction when a 10-mm boundary constraint was applied, and (c) shows the reconstruction when a 16-mm boundary constraint was applied. Figure 2(a) is over 50% different than the ground-truth, while 2(b) and 2(c) are only 6.07% and 6.34% different from the ground-truth respectively. The result supports the accuracy in estimating the lung elasticity for varying boundary constraints.

In summary, our elasticity estimation converged with about 99% sub-millimeter accuracy, resulting in an elastic convergence of about 92%. We have shown that the use of the locally heterogeneous convergence magnification approach is necessary in the transition to apply our conventional elastography technique to lung anatomy. However, use of different ground-truth elasticity distributions and different boundary constraint magnitudes did not affect the convergence of our technique. While we mainly focus on ground-truth values obtained from an elastodynamic forward model, “noisy” and elastostatic forward models also produced reliable elasticity estimations.

During Q4 of Y2, our work is summed up below.

Objectives: Liver diseases, such as liver cancer and cirrhosis, are commonly associated with changes in the biomechanical properties of liver tissue. Functional imaging techniques such as elastography have shown great promise in measuring the biomechanical properties of liver tissue; however, current liver elastography techniques require additional equipment that is not available within the radiotherapy setup. We present a novel methodology for estimating liver elasticity derived from deformation observed during 4DMR ViewRay (MRIdian System™, ViewRay™, Cleveland, OH, USA) scans within a radiotherapy setup.

Methods: Phase 1 and phase 8 datasets, categorized by diaphragm position, were deformably registered. The resulting displacement maps were considered ground-truth. A GPU-based biomechanical model was then assembled from the segmented phase 8 liver dataset and, along with patient-specific boundary constraints, used to iteratively solve for the liver elasticity distribution. The liver elastography process was performed for 11 4DMR patients.

Results: Maximum liver deformation was observed to be between 3.99 and 9.04 mm. On average, 95% convergence within 1 mm was observed. A validation study using phase 4 liver datasets illustrated an accuracy of 86%. Normalized cross-correlation quantified high similarity between the results of the estimation and validation studies with their respective ground-truths.

Conclusions: Overall, the results suggest that liver elasticity can be measured with approximately 95% convergence using 4DMR scans acquired within the radiotherapy workflow.

Advances in knowledge: These results indicate the potential for performing liver elastography within the radiotherapy setup without the need for additional equipment, which can lead to improved tissue-sparing radiotherapy treatment plans and more precise monitoring of treatment response.

Hepatocellular carcinoma (HCC) is one of the most common malignancies, and the third most common cause of cancer-related death worldwide.[1, 2] Surgical resection and liver transplantation are the primary treatment methodologies, however strict criteria limit the pool of eligible patients for both cases. HCC has a poor prognoses, with a 5-year survival rate of less than 12% due to a combination of late diagnosis and lack of efficient therapies for advanced stages.[3] Stereotactic body radiotherapy (SBRT) has been used to treat patients with HCC who are not eligible for other treatments.[4] SBRT uses advances in imaging and conformal radiotherapy to deliver ablative, high dose radiation in order to optimize local control. Radiation-induced liver disease (RILD) is a significant limiting factor in the use of SBRT because there are no effective treatments or predictors.[2] Most patients with HCC have pre-existing cirrhosis or hepatitis, which may significantly increase their risk of RILD.[5] Baseline liver function is thought to be the most important factor associated with risk of RILD.[1] Pre-treatment visualization of liver function in vivo is necessary in order to expand the use of SBRT for HCC.

The liver plays a role in metabolism, synthesis, secretion, immunity, and many other functions.[6] Liver disease, including cirrhosis, fibrosis and tumors, can disrupt the functions of the liver by altering the biomechanical properties of the tissue, most notably by changing the tissue stiffness.[7, 8] Clinically, elastography provides a measurement of liver stiffness and is a predictor for HCC.[9] Magnetic resonance elastography (MRE) can noninvasively and quantitatively assess the elasticity characteristics of soft tissue.[7] Liver stiffness measured by MRE has been shown to correlate well with histologic staging of fibrosis and differentiation of benign and malignant liver lesions.[10] However, current MRE techniques require equipment that is not typically available within a conventional radiotherapy setup.

Recently, an MR guided radiation therapy (MRgRT) system (MRIdian System™, ViewRay™, Cleveland, OH, USA) was introduced in the field of radiotherapy (RT).[11] The ViewRay system integrates a 0.35T MRI and 3 Cobalt sources, which allows for simultaneous MRI acquisition and treatment delivery for a variety of malignancies.[12] The superior soft tissue contrast from ViewRay's on-board MRI enables soft tissue based gated RT and also provides an effective way for on-line adaptive RT. Both techniques are especially helpful for treating thoracic and abdominal tumors by effectively accounting for intra-fractional and inter-fractional motion. In addition, a 4DMRI sequence on the 0.35T magnet on ViewRay was recently developed for motion characterization.[13] In this study, we present a novel elastography process for estimating liver tissue elasticity using 4DMRI to observe liver deformation in each respiratory cycle during patient treatment simulation. The rest of this paper is organized as follows: Section 2 introduces the methods employed for the deformable imaging registration, elasticity estimation, validation, and quantitative evaluation. Section 3 presents the qualitative and quantitative results of the deformable image registration, elastography, and validation processes. Section 4 presents a discussion of the results and highlights the areas for continued research, while section 5 concludes the paper.

Our elastography process focuses on estimating the effective Young's modulus for each voxel of liver tissue using 4DMR liver data. Figure 1 shows a flow chart summarizing the elasticity estimation. First, phase 1 and phase 8 datasets from the 4DMR liver images were registered using an optical flow deformable image registration (DIR) algorithm.[14] Liver deformation vectors (DVFs) were obtained for every voxel of liver tissue. The biomechanical model was then assembled using segmented phase 1 liver geometry and a randomly initialized elasticity distribution. Using the ground-truth liver DVFs, the elasticity distribution was optimized. The inverse elasticity problem was formulated as a parameter-optimization problem with an objective to determine the elasticity parameter that would minimize the difference between the ground-truth deformation and the deformation computed by a biomechanical model. The biomechanical model and inverse elasticity estimation was implemented on a GPU cluster, which allowed the elasticity estimation for each patient

dataset to converge in around 2 hours. Spatial elasticity and displacement error distributions were then obtained and validated.

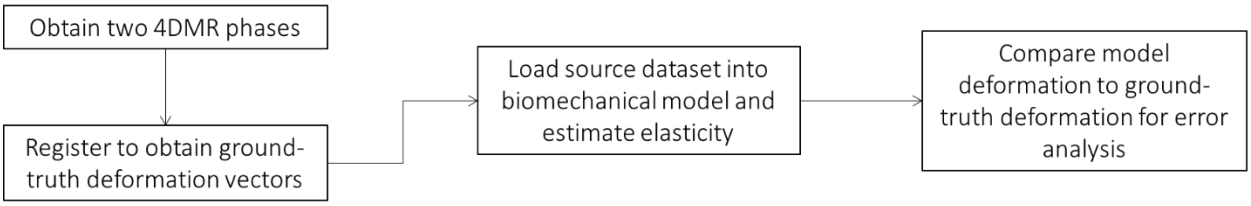


*Figure 1. Flow chart describing the liver elastography process. Two 4DMR liver phases are registered and ground-truth deformation vectors are obtained. A biomechanical model is used to obtain an optimal elasticity estimation and error analysis.*

In this section, we first briefly present the 4DMR acquisition process and the DIR technique used to obtain the ground-truth DVF. Next, we present the constitutive model and convergence criteria used for the elasticity estimation process. We then describe a technique that was used to validate the estimated elasticity. We conclude the section with a discussion of the metrics used to evaluate the quantitative accuracy of the elasticity estimation and validation results.

The study was approved by our institutional review board and each patient provided written informed consent. Eleven patients with tumors in the liver treated on ViewRay were included in our study. The MRI study was performed immediately after high resolution 3D MRI simulation acquisition. The 4DMRI sequence parameters are: TE/TR=3.0/6.0ms; bandwidth=400Hz/pixel; FA=110°, field-of-view=500x350x200mm, resolution=1.3x1.3x1.8mm$^3$, acquisition time = 7min. No specific breathing instruction was given to the subjects during the MRI exam.

The model-guided elasticity approach presented in this paper relies on displacement values extracted from DIR of 4DMR datasets. 4DMR datasets were acquired from 4DMR ViewRay (MRIdian System™, ViewRay™, Cleveland, OH, USA) scans taken within a radiotherapy setup. The 4DMR datasets were separated into phases according to diaphragm position. The liver was segmented and phase 1, corresponding to end inspiration, and phase 8 datasets, corresponding to end expiration, were then deformably registered using a well-validated in-house multi-level optical flow DIR algorithm.[14] The resulting DVFs were taken to be the ground-truth displacement for the elasticity estimation process. For the rest of the paper, the phase 8 datasets will be considered the source images, the phase 1 datasets will be considered target images, and the phase 8 datasets deformed according the ground-truth displacement will be considered warped images.

The accuracy of the DIR results is necessary to ensure the validity of the ground-truth deformation data. Figure 2 illustrates an example of the DIR for a 2D-slice of 4DMR data. Figure 2(a) shows the source data (phase 8 dataset) in red overlain with the target (phase 1) data in green. Mismatches can be seen between the source and target, especially near the diaphragm and liver boundaries. Figure 2(b) shows the target data is red overlain with the warped source data in green. It can be seen that the registration accounts for the liver deformation well, with little mismatch seen between the target and warp images. The extent of the registration accuracy will be further quantified in Section 3.4.

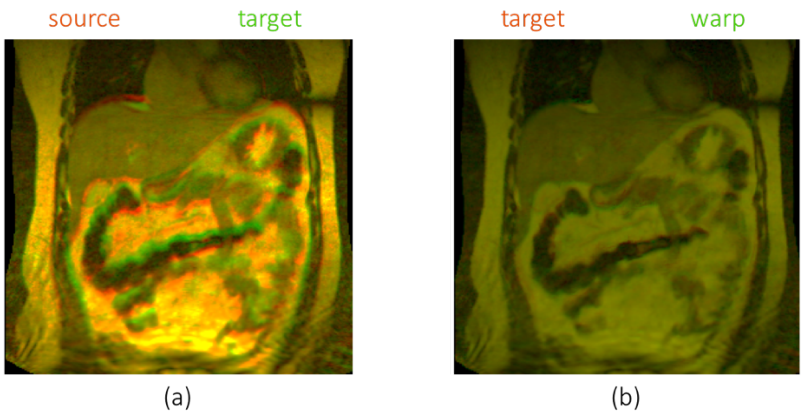


*Figure 1: Example of the registration results achieved with our in-house optical flow algorithm. The source (red) and target (green)(a) were registered, resulting in the warped (green) image that is overlain with the target in (b).*

4. Tissue properties measurement and validation

During Q1 of Y2, our work focused on developing a comprehensive experiment method to measurement the mechanical properties of ex vivo perfused and sectioned porcine liver. We are in regular contact with the modeling team to ensure our choice of measurements and methodologies (e.g., tissue sample choice, strain rates of measurement) are most applicable to their models.

A freshly harvested liver will be flushed with cold veterinary lactated ringer's solution before transporting to the room where the liver will be perfused and tested. The schematic of the perfusion system is shown in Figure 1. Six liters of a specific kind of perfusate (5L Dextrose 5% Lactated Ringers Solution and 1 L 6% Hetastarch solution[1]) will be pumped to two hydro-statically elevated reservoirs. The organ will be stabilized on a sturdy surface without submerging the organ. The temperature of the perfusate will be maintained at 39ºC which is the core temperature of a pig.

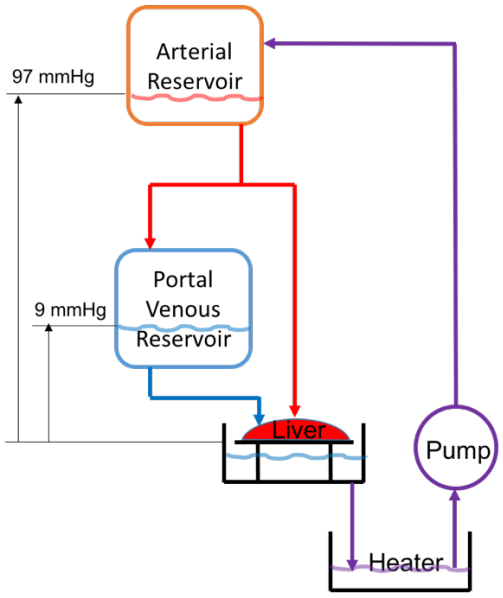


Figure 1 Schematic of the perfusion system.

The same testing instrument (300C Dual Mode Muscle Lever system, Aurora Scientific Inc., Canada) as mentioned in the Y1Q4 report was used to apply a compression force on the liver surface. The diameters of the probes were selected based on the statement from Zhang et al.[2]. The diameters were selected to be 5 mm and 6 mm for the indentation tests and stress relaxation/creep tests. The surface of the probe will be covered by fine grit sand paper to prevent relative motion at the interface.

Quasi-static indentation, indentation at different loading rates, stress relaxation and creep tests will be conducted on different lobes of the perfused liver. The surface of each lobe will be meshed to 25 mm x 25 mm grid and testing points are located in the center of each square (as shown in Figure 2). The natural thickness of each testing point will be measured and recorded before testing.


Figure 2 Testing points are shown on the surface of a porcine liver.

For quasi-static indentation tests conducted on one lobe of the perfused liver, the maximum strain will be 0.05 and the loading/unloading rate is 0.2 mm/s. The sample will be immediately unloaded once the displacement reaches the maximum value. Each testing points will be tested for three times and it will be allowed to recovery for 1 hour before the next measurement.
For indentation test at different loading rates conducted on another lobe of the perfused liver, the maximum strain will be 0.15 and the loading/unloading rates will be 1, 2, 5, 10, 20 and 50 mm/s. Three testing points, which are only located in the middle part of the lobe, are loaded at each rate only for one time.

For stress relaxation test conducted on another lobe of the perfused liver, the maximum strain will be 0.2 and the loading rate is 10 mm/s. For creep tests conducted on the same lobe of the perfused liver, the loading rate is the same and the maximum load will be chosen from 0.1, 0.2, 0.5, 0.7, 1, 1.25, 1.5, 2, 2.5 and 3 N based on the force data measured in the previous tests to prevent the liver from damage. The waiting time for both tests will be 300 sec. And three testing points from the middle and edge part of the lobe will be tested in each kind of experiment.

After all the tests are done on the perfused liver, the liver will be sectioned into small cubes along the lines of the 25 mm x 25 mm grid. So same testing points are tested after the perfusion system is removed from the liver. The procedures of those four kinds of tests mentioned above for sectioned liver tissue samples are the same as above. According to the opinions from our modeling group, we will submerge the tissue sample in the perfusate to take the possible poroelasticity of the liver into consideration. And the schematic of that

experiment setup is shown in Figure 3. We will also explore the anisotropic properties of parenchyma by removing the Gibson capsule and conduct indentation tests in all three directions.

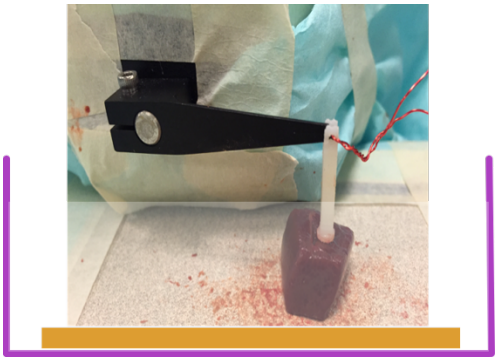

Figure 3 Schematic of experiment setup used for sectioned liver samples.

During Q2 of Y2, our work focused on conducting quasi-static indentation tests on perfused and sectioned liver tissue. We are in regular contact with the modeling team to ensure our choice of measurements and methodologies (e.g., tissue sample choice, strain rates of measurement) are most applicable to their models.

A liver, which weighed 918 g, was perfused with 5 liters of 39ºC normal saline solution within 2 hours of removal from a female pig (as shown in Figure 1).

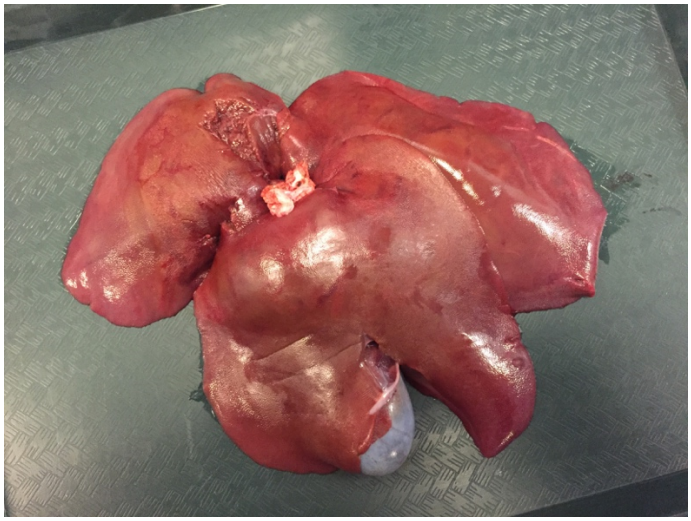

Figure 1 Picture of the liver used in our experiment.

The experiment setup of the perfusion system is shown in Figure 2.

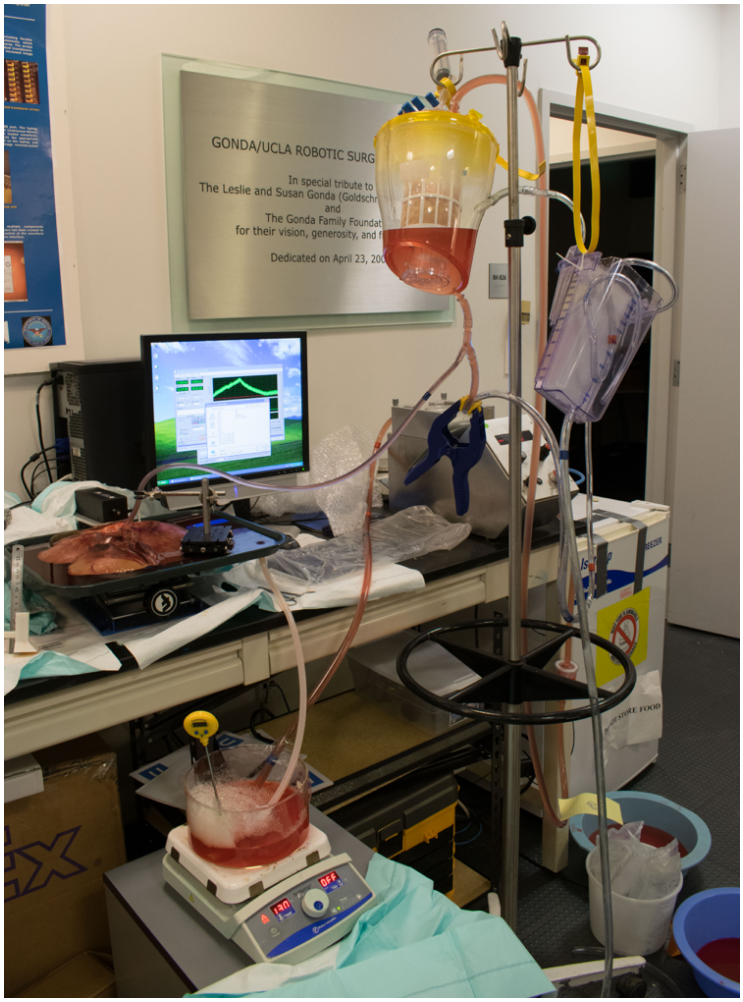


Figure 2 Picture of the perfusion system.

After all quasi-static indentation tests were done on the perfused liver, the perfusion system was removed from the liver. The liver was stored in a fridge at 4 ºC for 16 hours before further action was taken. All tests were conducted on the right lobe of the liver shown in Figure 1. That lobe was sectioned to small cubes along the lines of 25 mm x 25 mm grid. The sectioned liver samples are shown in Figure 3.

During the experiment, all samples are submerged in the normal saline The experiment setup of the sectioned liver sample is shown in Figure 4.


Figure 3 Picture of the sectioned liver tissue samples. Samples are label as (i, j) where i is the row number and j is the column number.

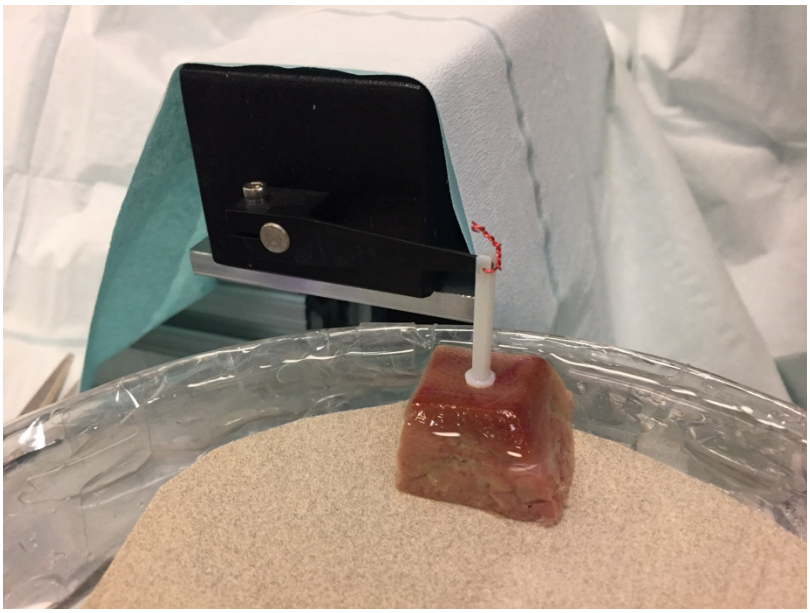

Figure 4 Picture of the experiment setup of sectioned liver samples.

In quasi-static indentation tests, the maximum strain was 0.05 and the loading/unloading rate was 0.2 mm/s. The sample was immediately unloaded once the displacement reached the maximum value. Each testing points were tested for 2 times when the liver was perfused and 3 times for sectioned liver samples. All testing points was allowed to recovery for 1 hour before the next measurement.

The hysteretic force-displacement curves of each testing point of perfused liver and sectioned liver are shown in Figure 5 and Figure 6 respectively. We can see that the sectioned liver tissue became stiffer as the number of test time went up because the liquid inside the sample was squeezed out and tissue was stick to each other during the tests. We inspected and recorded the diameters of the maximum vessels in the samples. And one thing to note is that all sectioned tissue samples had vessels inside the parenchyma. However, changes in mechanical properties cannot be easily told from those curves of the perfused liver tissue.

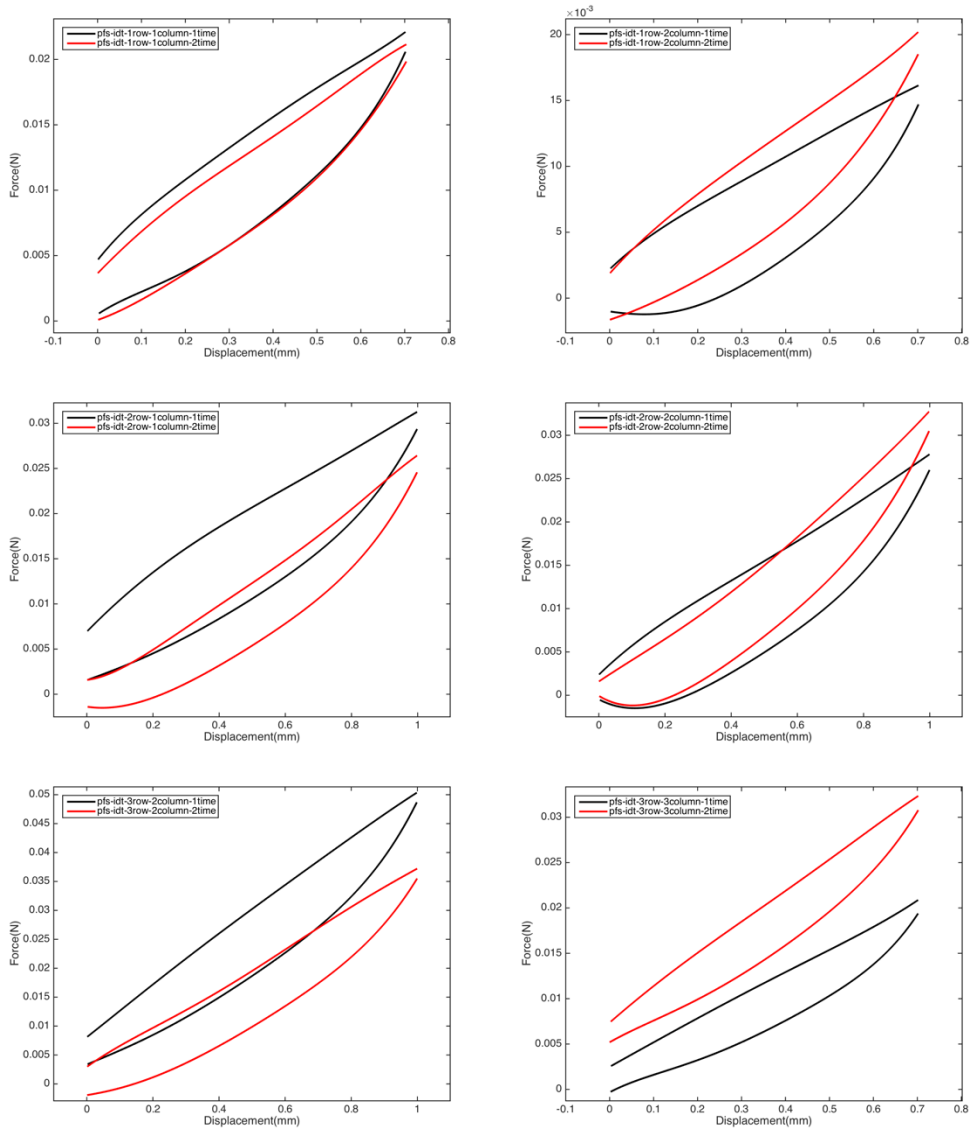

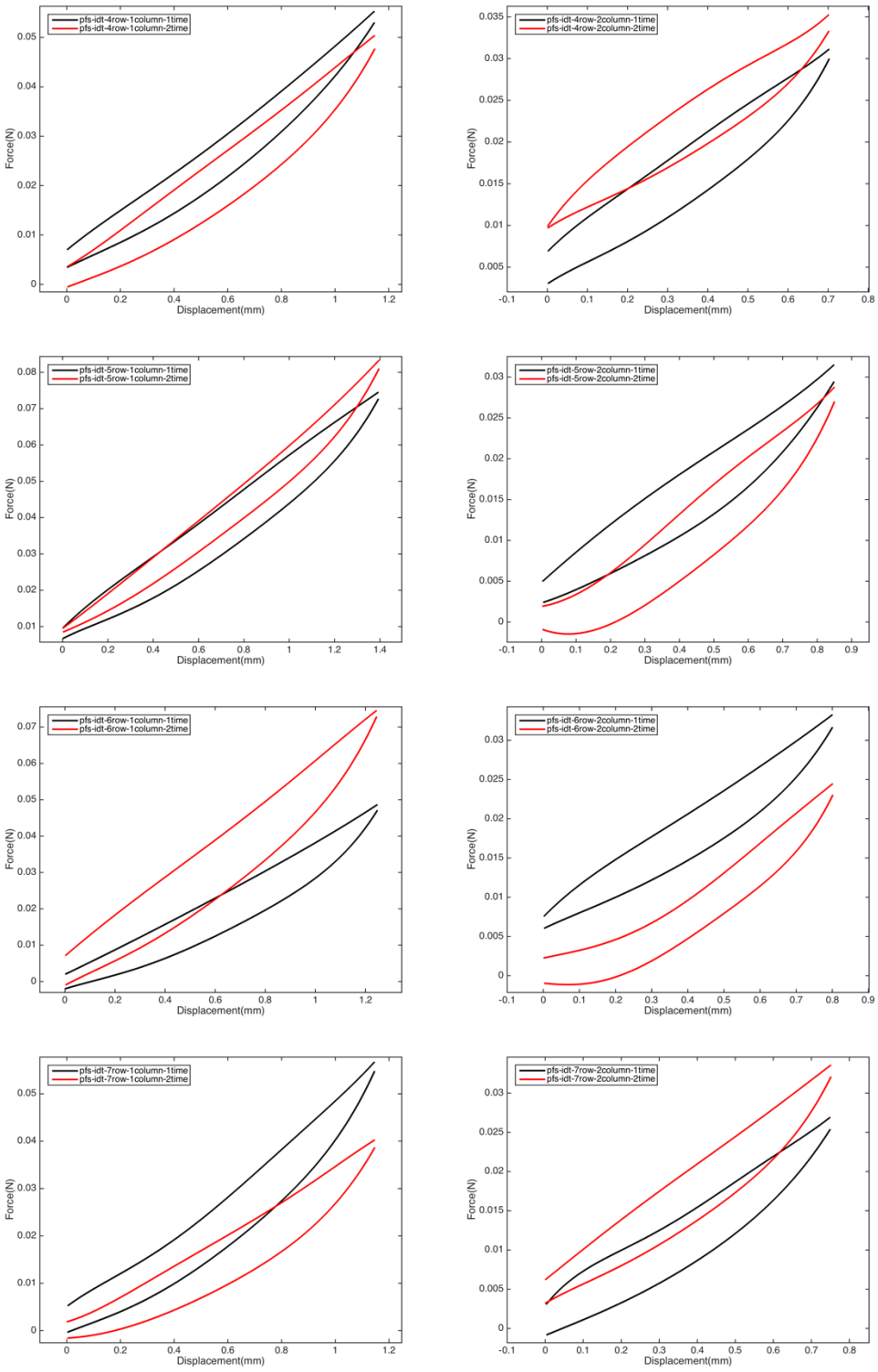


Figure 5 Hysteretic force-displacement curves of indentation tests on the perfused liver.

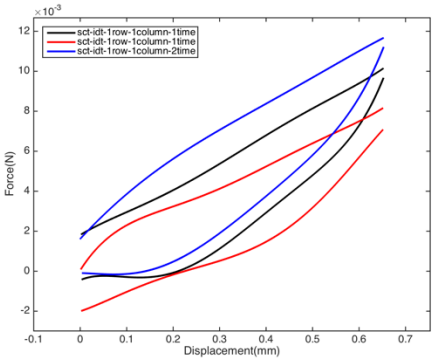
×10-3
sct-idt-1row-1column-1time
sct-idt-1row-1column-1time
sct-idt-1row-1column-2time
Force(N)
Displacement(mm)

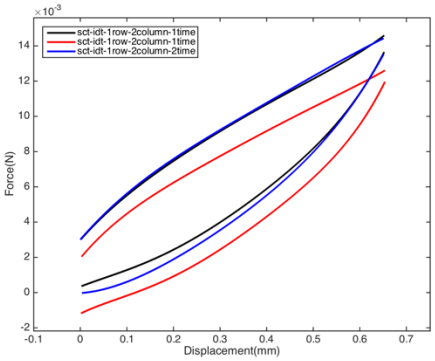
×10-3
sct-idt-1row-2column-1time
sct-idt-1row-2column-1time
sct-idt-1row-2column-2time
Force(N)
Displacement(mm)

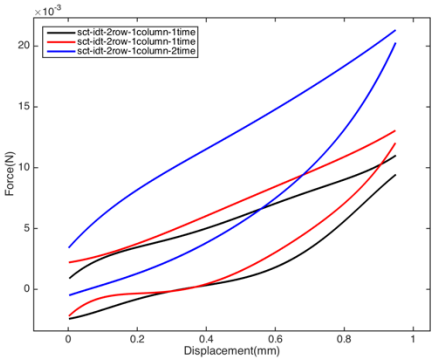
×10-3
sct-idt-2row-1column-1time
sct-idt-2row-1column-1time
sct-idt-2row-1column-2time
Force(N)
Displacement(mm)

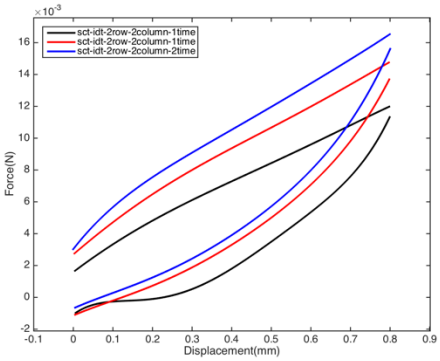
×10-3
sct-idt-2row-2column-1time
sct-idt-2row-2column-1time
sct-idt-2row-2column-2time
Force(N)
Displacement(mm)

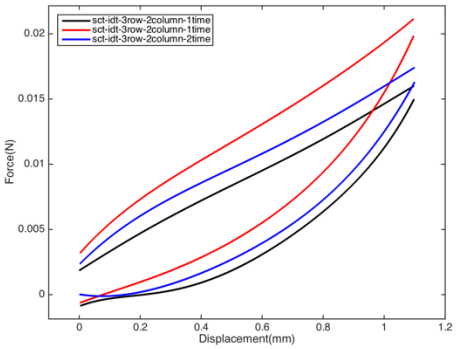
sct-idt-3row-2column-1time
sct-idt-3row-2column-1time
sct-idt-3row-2column-2time
Force(N)
Displacement(mm)

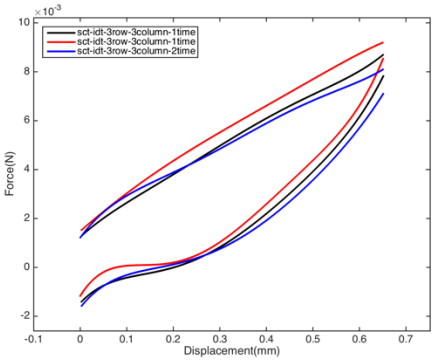
×10-3
sct-idt-3row-3column-1time
sct-idt-3row-3column-1time
sct-idt-3row-3column-2time
Force(N)
Displacement(mm)

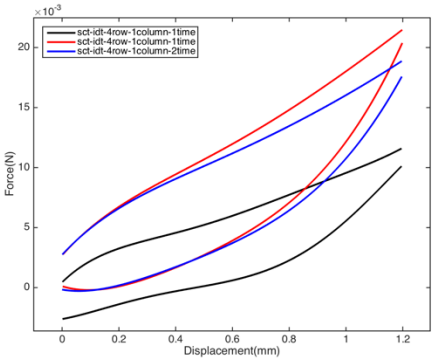
×10-3
sct-idt-4row-1column-1time
sct-idt-4row-1column-1time
sct-idt-4row-1column-2time
Force(N)
Displacement(mm)

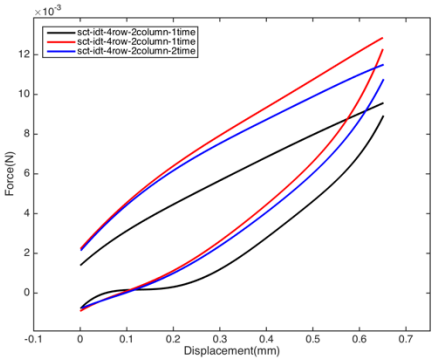
×10-3
sct-idt-4row-2column-1time
sct-idt-4row-2column-1time
sct-idt-4row-2column-2time
Force(N)
Displacement(mm)

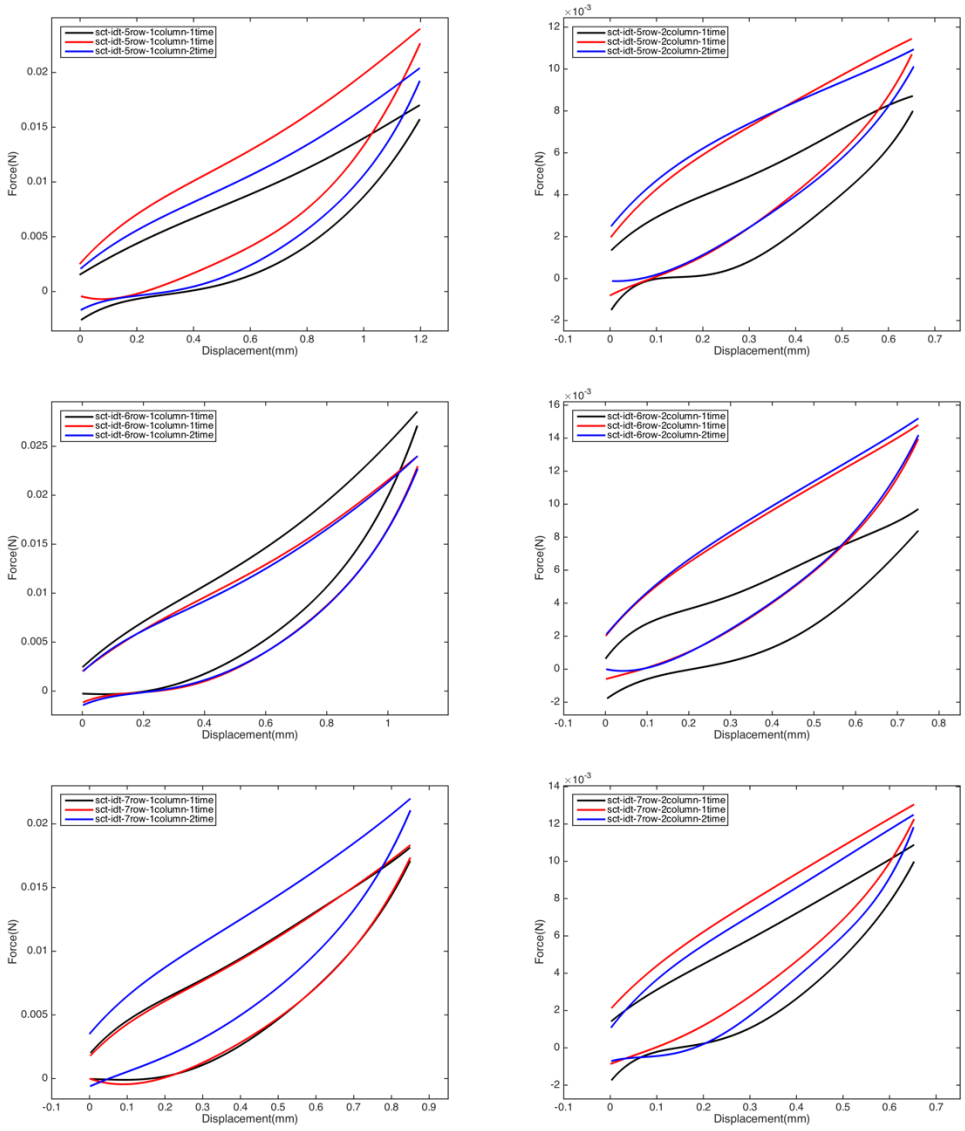


Figure 6 Hysteretic force-displacement curves of indentation tests on the sectioned liver samples.

We took the average value of the data collected from the 2 or 3 times measurements and summarized them in Figure 7 and Figure 8. We can see that perfused tissue was much stiffer and more linear than sectioned tissue.

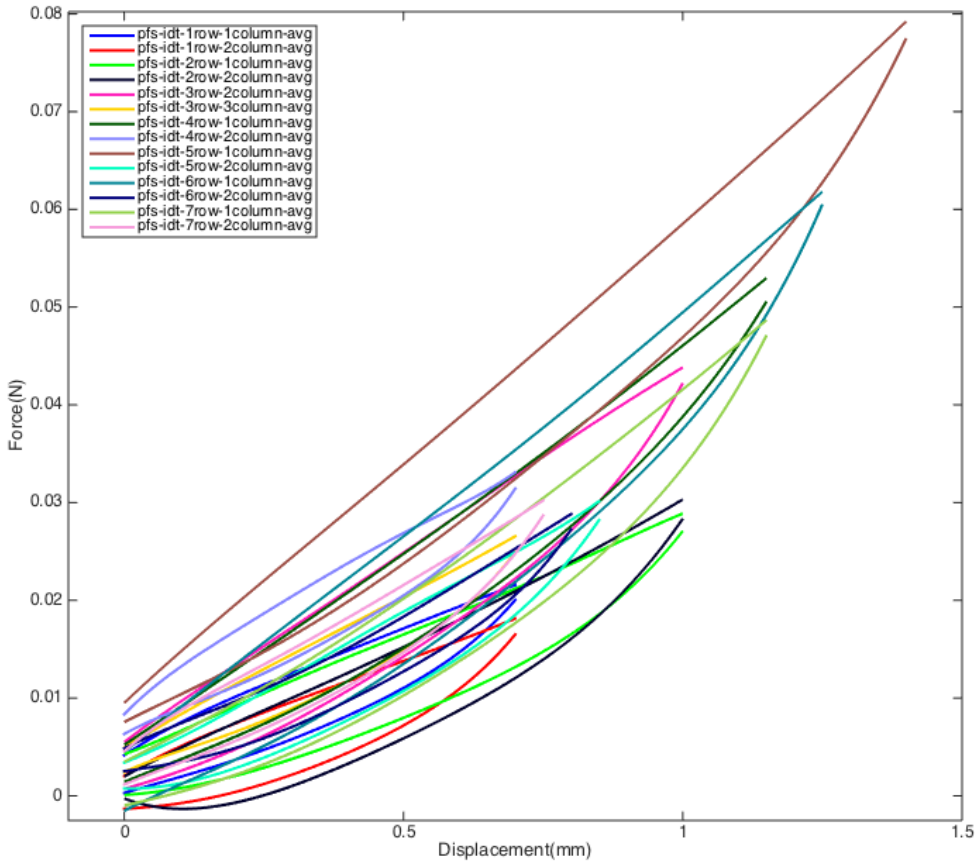


Figure 7 Hysteretic force-displacement curves of indentation tests at all testing points on the perfused liver.

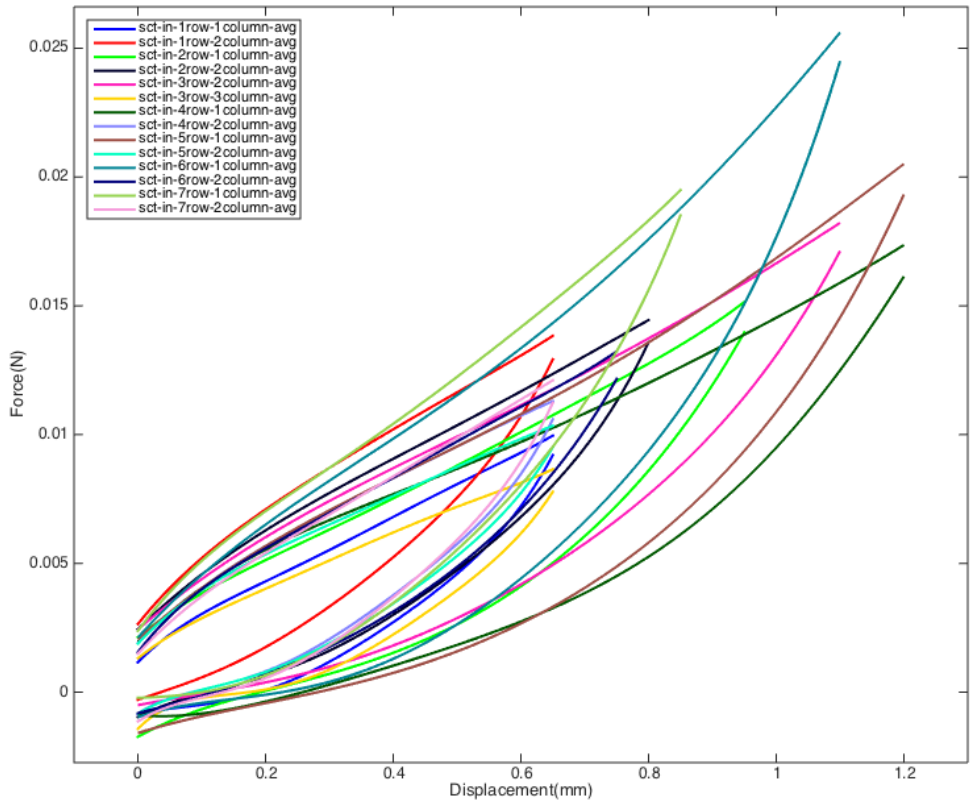

Figure 8 Hysteretic force-displacement curves of indentation tests at all testing points on the sectioned liver samples.

During the experiment, the diameter of the probe was 5mm. And by dividing the displacement by the natural thickness measured before each test, the hysteretic stress-strain curves of all testing points are summarized in Figure 9 and Figure 10. As it was mentioned before, the maximum strain for all tests was 0.05 and the loading and unloading processes were quasi-static. We can see from those figures that the tissue from the middle part of the liver is much stiffer than those from the edge part of the liver.

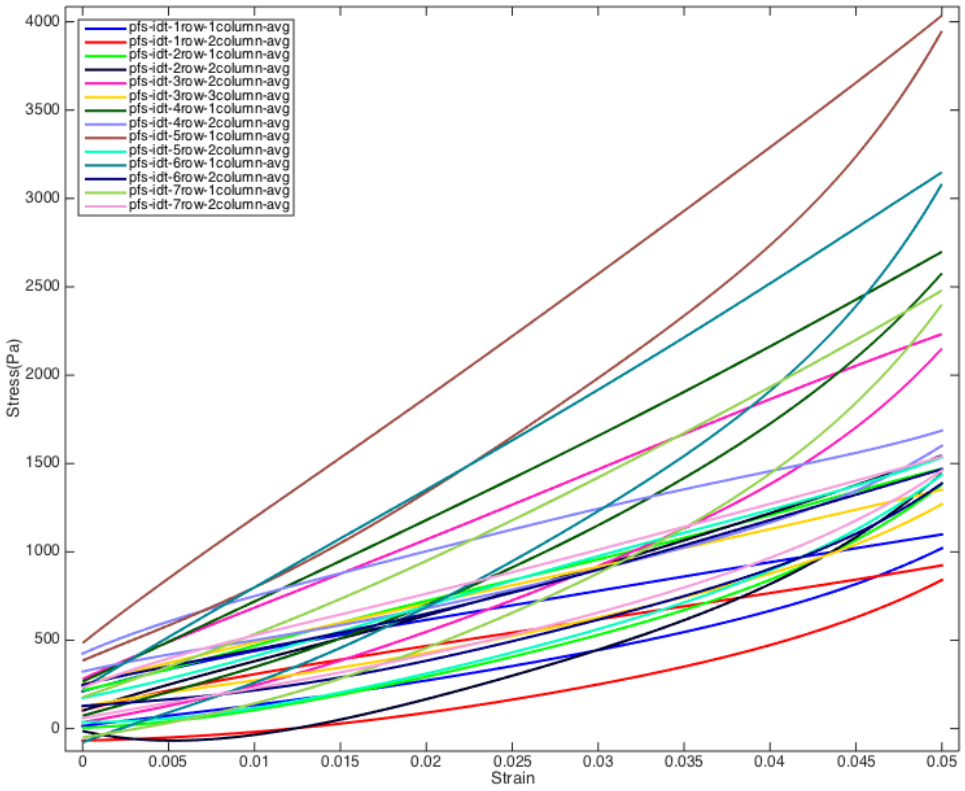


Figure 9 Hysteretic stress-strain curves of indentation tests at all testing points on the perfused liver.

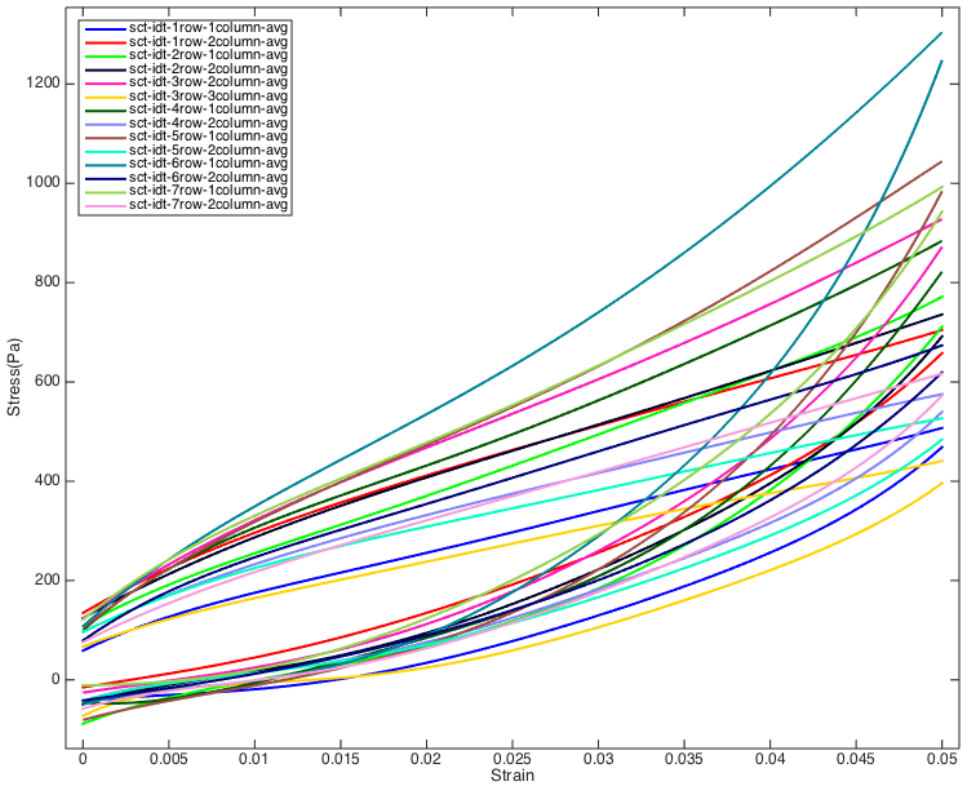


Figure 10 Hysteretic stress-strain curves of indentation tests at all testing points on the sectioned liver samples.

During Q3 of Y2, our work focused on conducting dynamic indentation tests on perfused and sectioned liver tissue. We are in regular contact with the modeling team to ensure our choice of measurements and methodologies (e.g., tissue sample choice, strain rates, relaxation, etc.) satisfies the requirements of the model development team.

A second liver, which weighed 1.05 kg, was perfused with 5 liters of 39 ºC normal Plasma-Lyte A Injection solution within 2 hours of removal from a female pig (as shown in Figure 1).

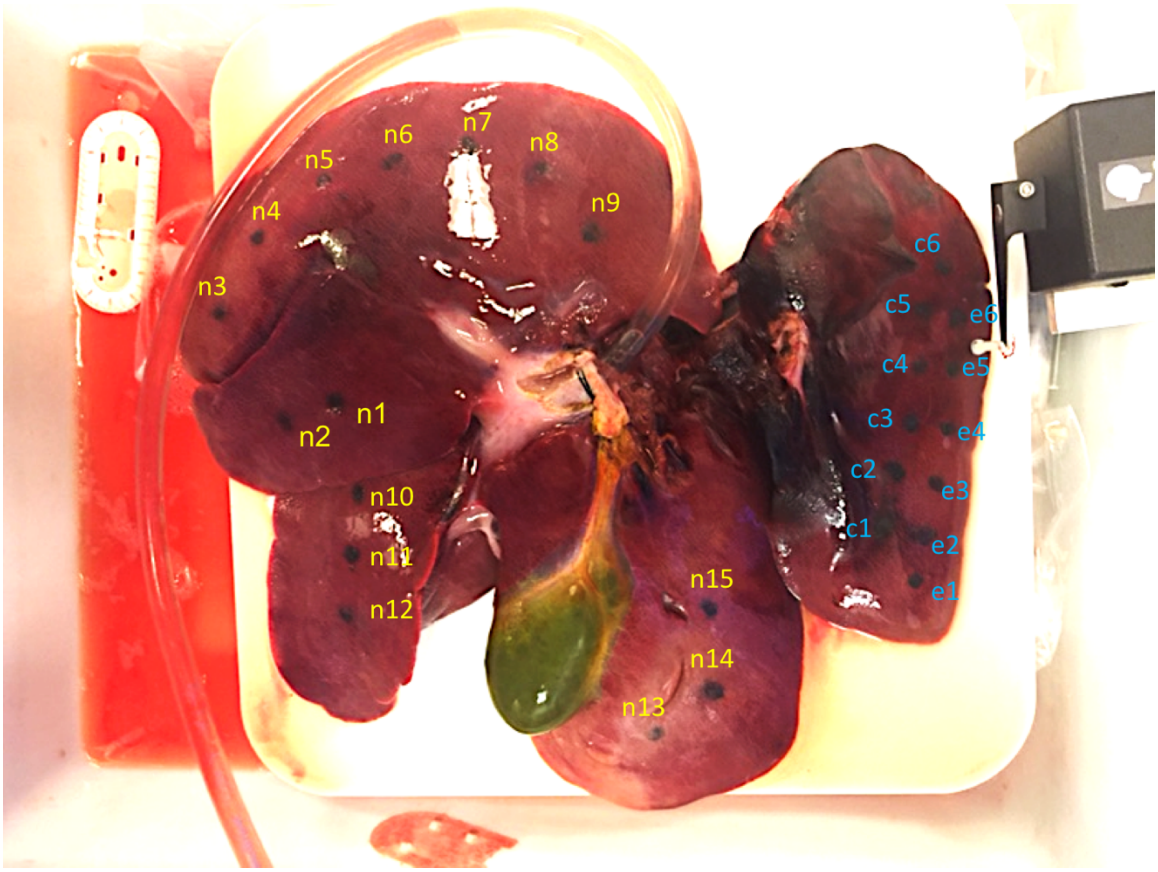


Figure 1 Picture of the perfused liver used in our experiment. Testing points used in indentation tests at different loading rates are labeled with yellow texts. And testing points used in stress relaxation and creep tests are labeled with blue texts.

The experiment setup of the perfusion system is shown in Figure 2. A probe with 5 mm in diameter was used in all measurements.

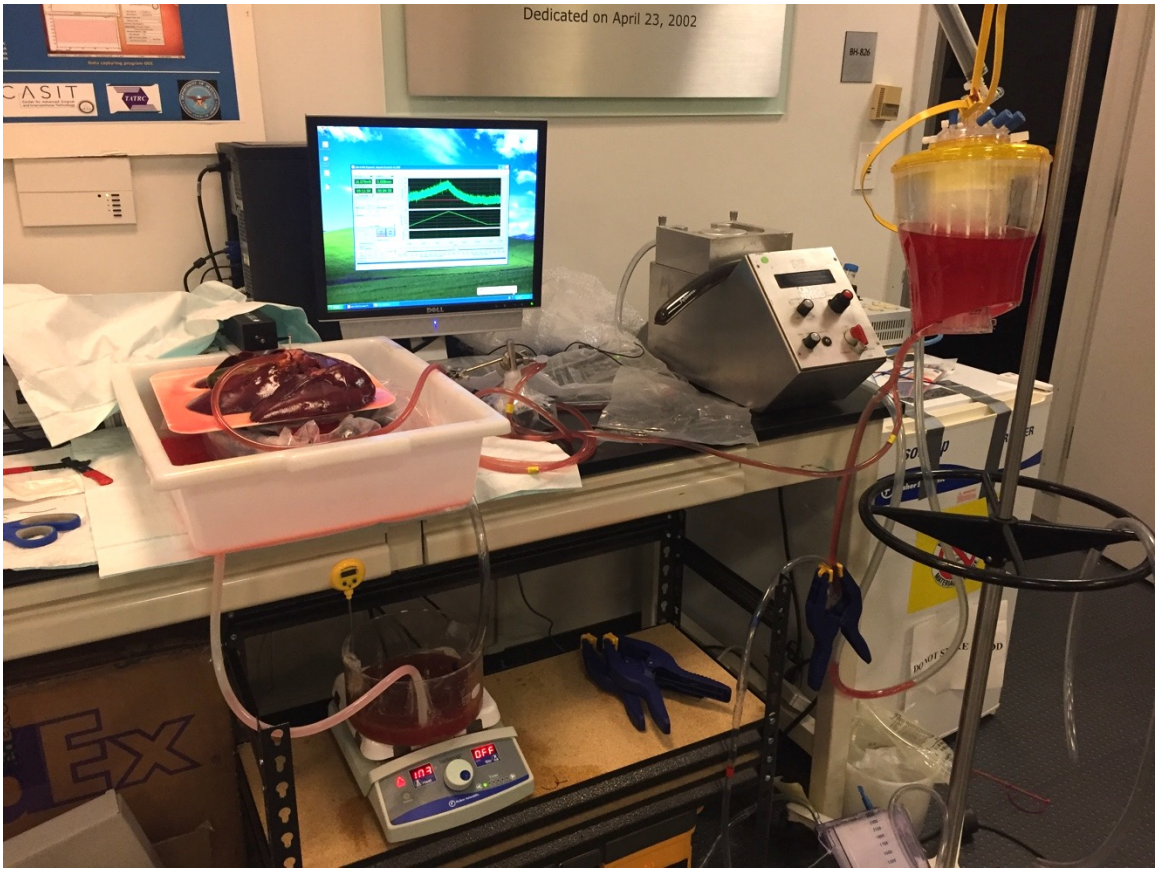


Figure 2 Picture of the perfusion system. The portal venous reservoir was elevated at 122 mm (9 mm Hg) above the top surface of the liver.

After all dynamic indentation tests were done on the perfused liver, the perfusion system was removed from the liver. The liver was stored in a refrigerator at 4 ºC for 12 hours prior to any additional experiments. All testing points are shown in Figure 1. Testing points for indentation, and relaxation and creep testing were sectioned into small cubes with a top surface area of 25 x 25 $mm^2$ and 10 x 10 $mm^2$, respectively.

During the experiment, all samples were submerged into normal Plasma-Lyte A Injection solution at room temperature. The experiment setup of the sectioned liver sample is the same as that used in quasi-static indentation tests at different locations as shown in the Year1 Quarter 6 report.

In indentation tests at different loading rates, the maximum strain was 0.3. Three testing points from n1 to n15 were loaded/unloaded at 1, 2, 5, 10, and 20 mm/s respectively. The sample was immediately unloaded once the displacement reached the maximum value. Each testing point was tested for 3 times when the liver was perfused and was tested for 3 times again when that location was sectioned. All testing points were allowed to recovery for 30 minutes before the next measurement.

We took the average of all measurements of all three testing points with the same loading/unloading rates and fitted them to the following Ogden model (two constants) with $R^2$>0.95,

$$\sigma^{eng} = \mu\left((1-\varepsilon)^{\alpha-1} - (1-\varepsilon)^{-\frac{1}{2}\alpha-1}\right) \qquad (1)$$

where $\sigma^{eng}$ is engineering stress, $\varepsilon$ is engineering strain, $\mu$ and $\alpha$ are material constants. The hysteretic stress-strain curves of different loading rates of the perfused and sectioned liver samples are shown in Figure 3 and Figure 4 respectively. The material constants and energy lost density of each curve are summarized in Table 1. We can see that the liver tissue became stiffer as the loading rate went up because of its viscoelastic properties. We inspected and recorded the diameters of the maximum vessels in the samples. And one thing to note is that all sectioned tissue samples had vessels inside the parenchyma.

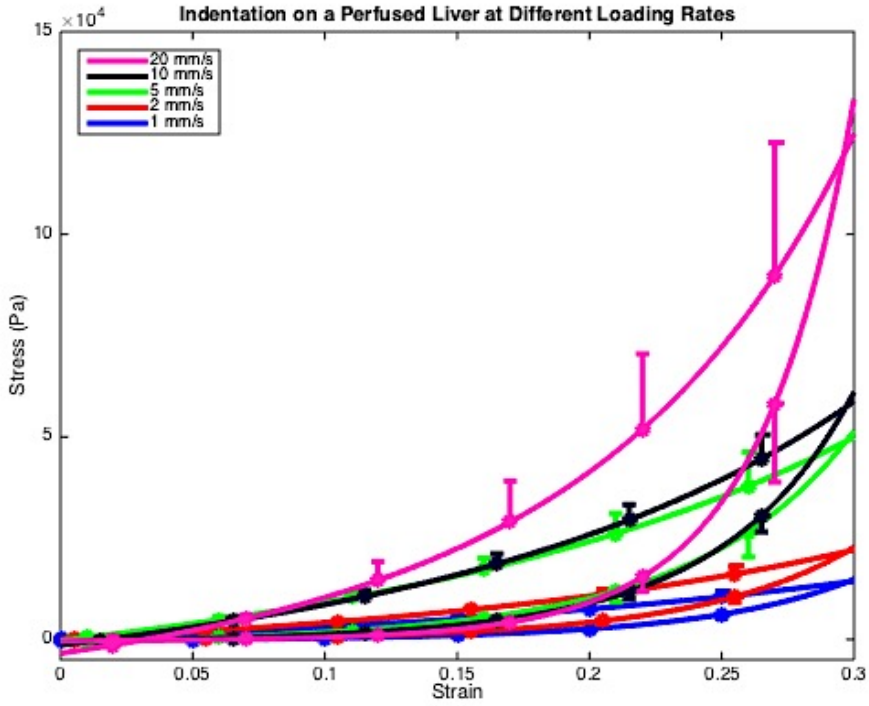


Figure 3 Hysteretic stress-strain curves of indentation tests at different loading rates on the perfused liver.

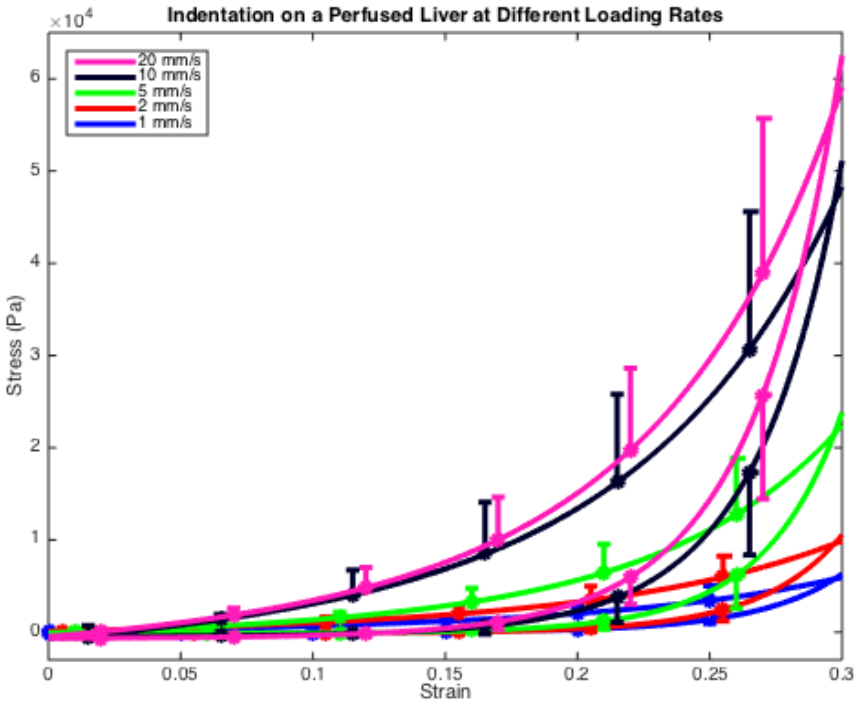


Figure 4 Hysteretic stress-strain curves of indentation tests at different loading rates on the sectioned liver samples.

Table 1 Parameters of the Ogden model representing indentation experimental data and energy lost density of each hysteresis curve.

| Loading/ Unloading Rate (mm/s) | Perfused Liver | | | | | Sectioned Liver Samples | | | | |
|---|---|---|---|---|---|---|---|---|---|---|
| | Loading | | Unloading | | Energy Lost Density ($J/m^3$) | Loading | | Unloading | | Energy Lost Density ($J/m^3$) |
| | $\mu$ | $\alpha$ | $\mu$ | $\alpha$ | | $\mu$ | $\alpha$ | $\mu$ | $\alpha$ | |
| 1 | 1.19e4 | -1.36 | -199.42 | 22.33 | 801.95 | 374.86 | -6.77 | -2.84 | 41.26 | 261.85 |
| 2 | 8.81e3 | -2.45 | -332.37 | 21.84 | 1.04e3 | 613.66 | -6.84 | -2.96 | 43.92 | 420.27 |
| 5 | 2.16e4 | -2.32 | -845.97 | 21.14 | 2.17e3 | 659.21 | -8.92 | -4.50 | 46.11 | 646.78 |
| 10 | 1.54e4 | -3.33 | -417.23 | 26.01 | 2.41e3 | 2.11e3 | -7.86 | -21.54 | 41.63 | 1.47e3 |
| 20 | 1.05e4 | -6.13 | -119.16 | 37.39 | 4.13e3 | 1.89e3 | -8.70 | -38.12 | 39.57 | 1.61e3 |

From Table 1, the relationships between parameters ($\mu, \alpha$) and loading/unloading rates are hard to tell (Figure 5).

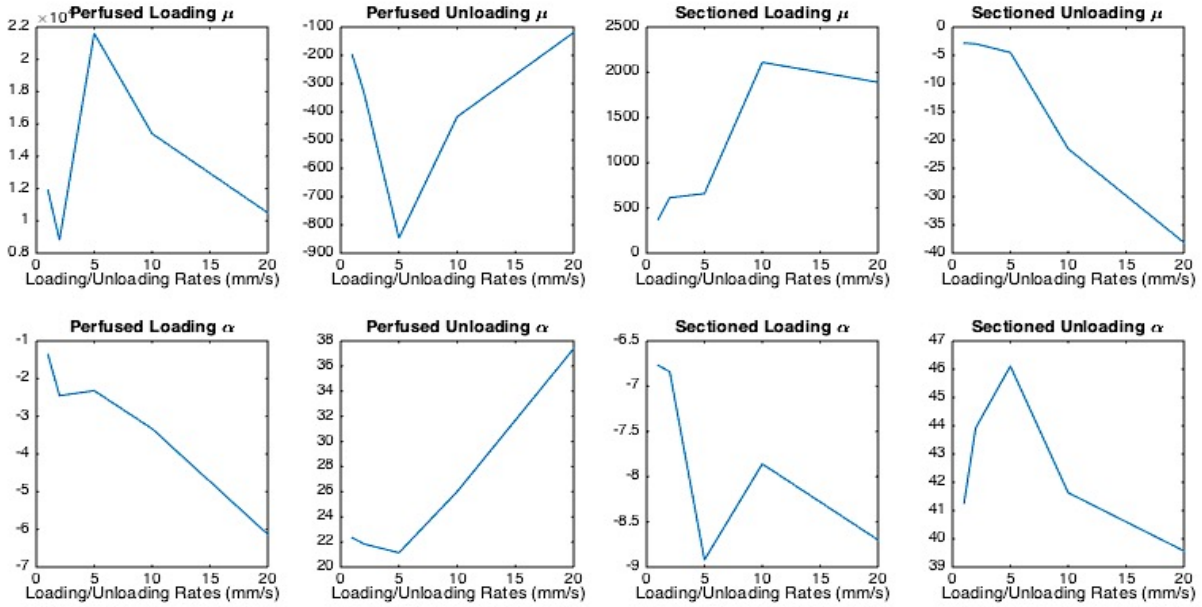


Figure 5 Relationships between parameters (μ, α) and loading/unloading rates on the perfused and sectioned liver samples.

However, we notice from Equation (1) that $\mu \times \alpha$ becomes a new parameter when we take the first derivative of $\varepsilon$ and $\alpha \gg 1$. Therefore, we fitted $\mu \times \alpha$ with loading/unloading rate to a quadratic function (Equation (2)) and the results are shown in Figure 6 and Table 2.

$$y = a_2 x^2 + a_1 x + a_0 \qquad (2)$$

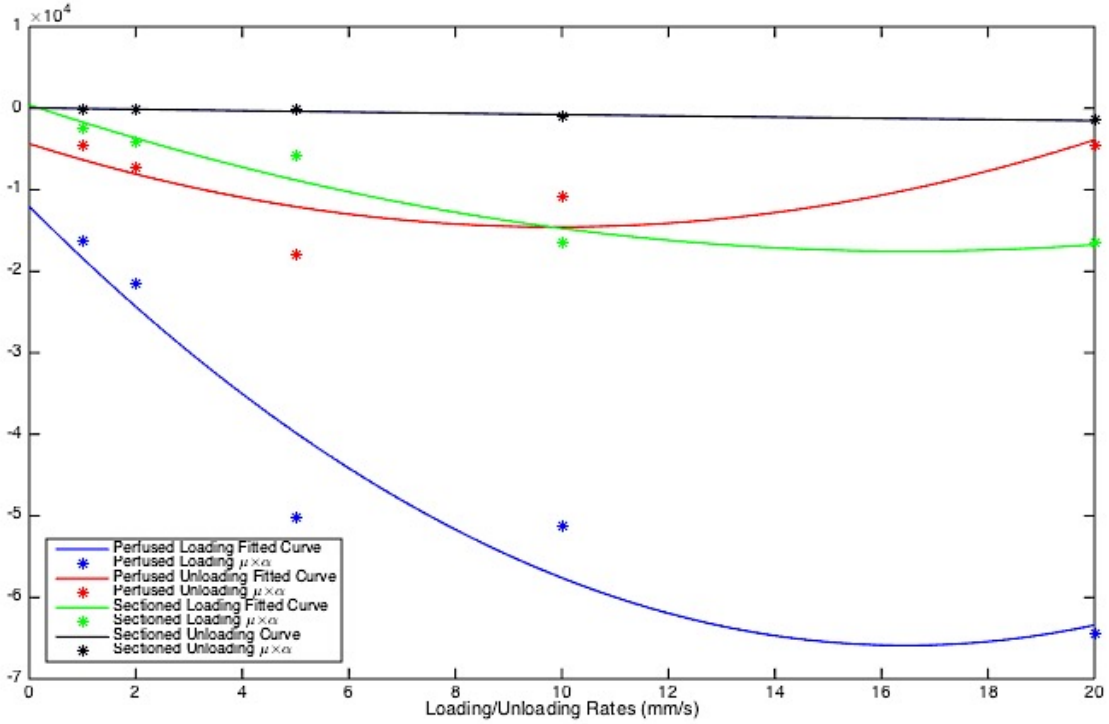


Figure 6 Relationships between the product $(\mu \times \alpha)$ and loading/unloading rates on the perfused and sectioned liver samples.

Table 2 Coefficients in Equation (2) representing the relationships between the product $(\mu \times \alpha)$ and loading/unloading rates on the perfused and sectioned liver samples

| Coefficients | Perfused Liver | | Sectioned Liver | |
|---|---|---|---|---|
| | Loading | Unloading | Loading | Unloading |
| $a_2$ | 198.89 | 104.46 | 65.78 | 0.41 |
| $a_1$ | -6545.37 | -2065.26 | -2172.67 | -86.60 |
| $a_0$ | -12042.77 | -4357.74 | 410.55 | 43.18 |

Since a limit of energy lost density mush exist for a given loading process, we fitted the energy lost density with loading/unloading rate to a logarithmic function (Equation (3)) and results are shown in Figure 7 and Table 3.

$$y = b_1 log x + b_0 \quad (3)$$

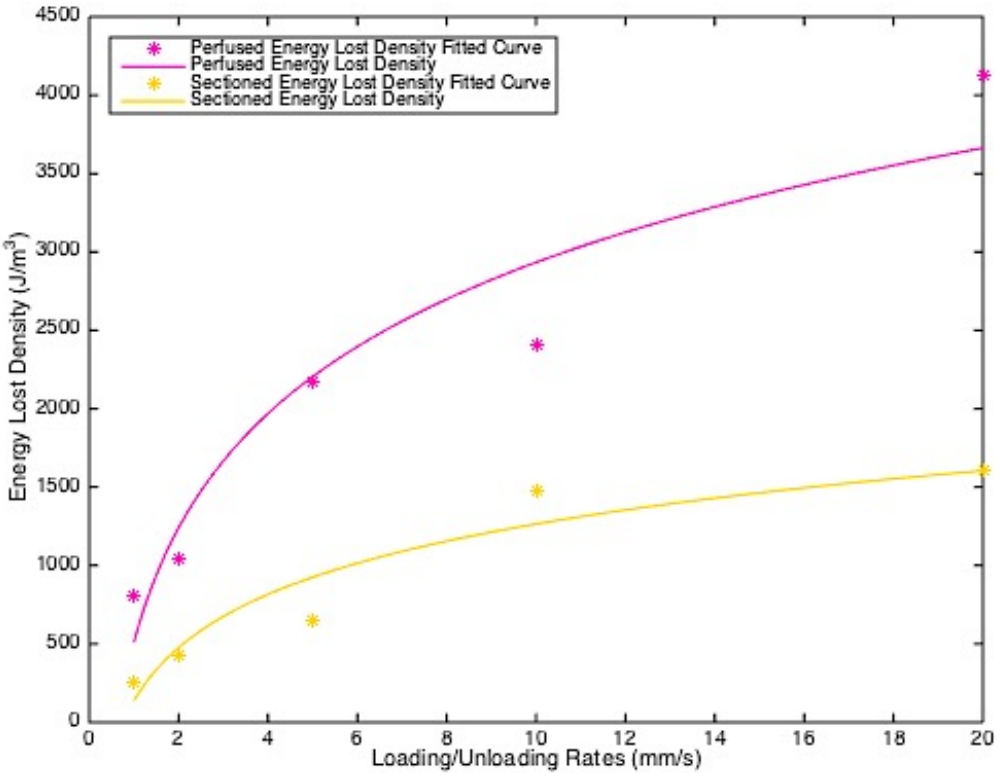


Figure 7 Relationships between the energy lost density and loading/unloading rates on the perfused and sectioned liver samples.

Table 3 Coefficients in Equation (3) representing the relationships between the energy lost density and loading/unloading rates on the perfused and sectioned liver samples.

| Coefficients | Perfused Liver | Sectioned Liver |
|---|---|---|
| $b_1$ | 1052.0 | 489.9 |
| $b_0$ | 511.0 | 137.0 |

In stress relaxation testing, the maximum strain was kept at 0.3. Three testing points (e1, e3, and e5) from the edge part of a lobe and three testing points (c1, c3, and c5) from the center part of a lobe (Figure 1) were loaded at 10 mm/s and the change of force was measured for 300 sec. Each testing point was only tested for one time when the liver was perfused and sectioned.

The experimental data of stress relaxation tests of the perfused liver and sectioned liver samples are shown in Figure 8. One thing to note is that some sectioned samples, especially the samples in the center part of the lobe, were too thick (30 mm verses the length of top surface which is 10 mm) to stand stably during the 300-sec measurement period. For this reason, we failed to collect data from those samples.

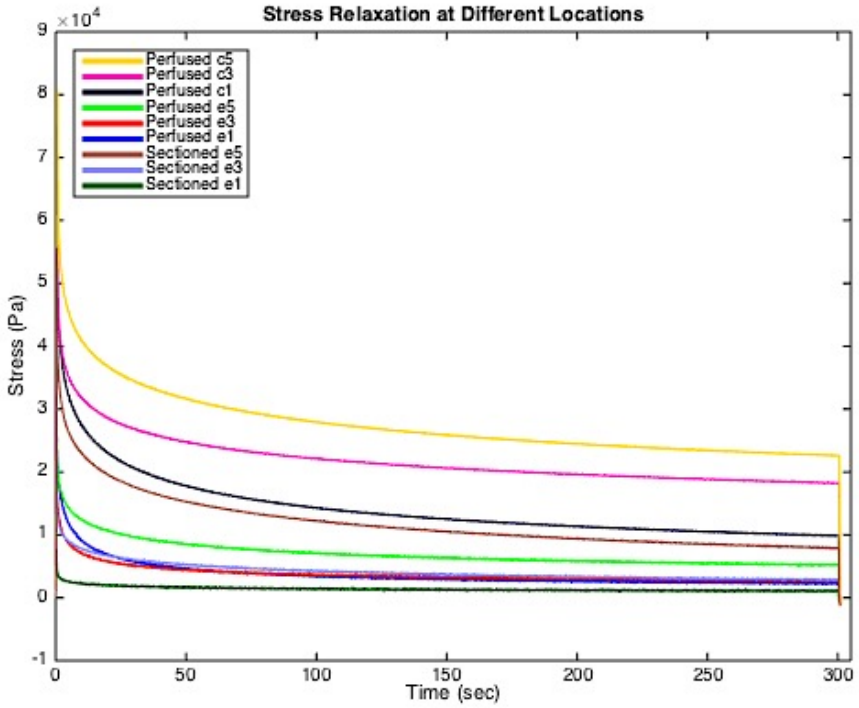


Figure 8 Experimental data of stress relaxation tests at testing points from the center and edge parts of a lobe when the liver was perfused and sectioned.

In creep testing, the maximum force was kept at 0.3 N. Three testing points (e2, e4, and e6) from the edge part of a lobe and three testing points (c2, c4, and c6) from the center part of a lobe (Figure 1) were loaded at 10 mm/s and the change of displacement to maintain the maximum force was measured for 300 sec. Each testing points was only tested for one time when the liver was perfused and sectioned.

The experimental data of creep tests of the perfused liver and sectioned liver samples are shown in Figure 9. However, some testing points, especially those in the center part of the lobe, were too slippery to hold the probe during the 300-sec period of measurement. Therefore, we failed to collect data from those testing points.

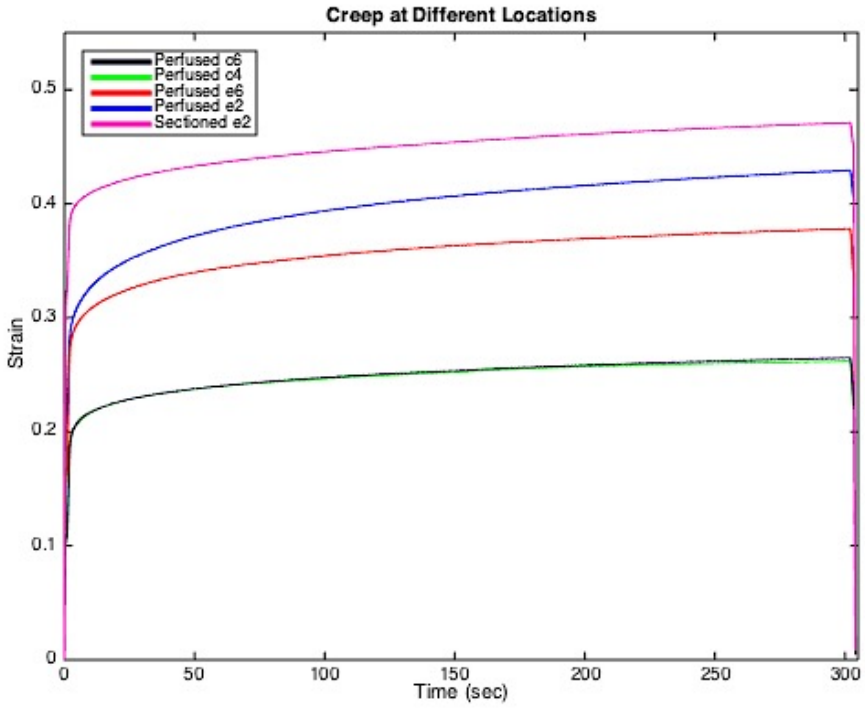


Figure 9 Experimental data of creep tests at testing points from the center and edge parts of a lobe when the liver was perfused and sectioned.

During Q4 of Y2, our work focused on conducting dynamic indentation tests on perfused liver tissue to figure out differences in mechanical properties between different lobes. We are in regular contact with the modeling team to ensure our choice of measurements and methodologies (e.g., tissue sample choice, fixing method, confinement, etc.) satisfy the requirements of the model development team.

A porcine liver consists of 5 lobes (as shown in Figure 1): four large lobes (right lateral lobe, right medial lobe, left medial lobe, and left lateral lobe) and one small lobe (caudate lobe). However, differences in mechanical properties between different lobes of a liver have been rarely reported. To the best of our knowledge, only Mattei et al. mentioned that the bulk compressive modulus (λ) of porcine fresh liver does not change significantly with the sample harvesting site (i.e. different liver lobes) nor between animals from the same slaughterhouse[1]. But they did not show in detail how they get this conclusion. So, it is still an important factor that should be seriously taken into consideration before any other tests are done on different lobes.

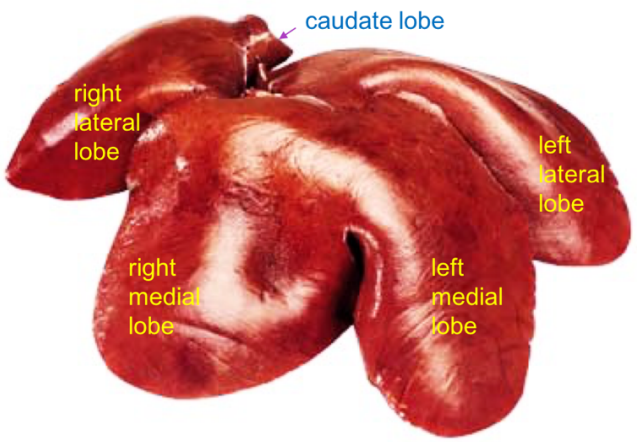


Figure 1 Picture of a porcine liver[2]

A liver, which weighed 0.91 kg, was perfused with 5 liters of 39 ºC normal Plasma-Lyte A Injection solution within 2 hours of removal from a female pig (as shown in Figure 2).

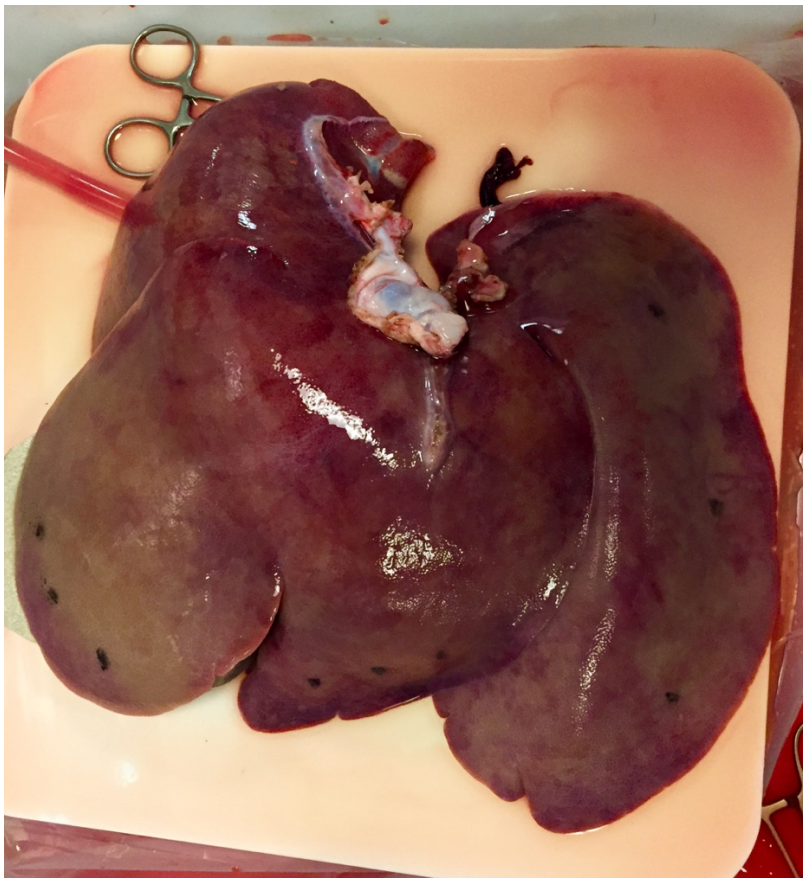

Figure 2 Picture of the perfused liver used in this experiment. Testing points used in indentation tests on different lobes are labeled with black points.

The experiment setup of the perfusion system is the same as we mentioned in the Year 2 Quarter 7 report. A cylindrical indenter with 5 mm diameter was used in all measurements.

In indentation tests on different lobes, the maximum strain was 0.3. Three points were tested at the edge and center part of each lobe. All testing points were loaded/unloaded at 1 mm/s. The sample was immediately unloaded once the displacement reached the maximum value. Each testing location was tested 3 times while the liver was perfused. All testing locations were allowed to recovery for 1 minute before the next measurement.

We took the average of all measurements of all three testing locations on the same part of the same lobe and fitted them to the Ogden model (two constants) (see Year2 Quarter 7 report Equation (1)) with $R^2$>0.95.

The hysteretic stress-strain curves of different lobes of the perfused liver are shown in Figure 3. The material constants and lost energy density of each curve are summarized in Table 1. We can see that the mechanical properties of the edge parts of a liver do not vary much with different lobes. However, mechanical properties of the center parts of a liver do vary a lot between different lobes since the structures, dimensions, and quantities of vessels varied a lot in the center part of different lobes.

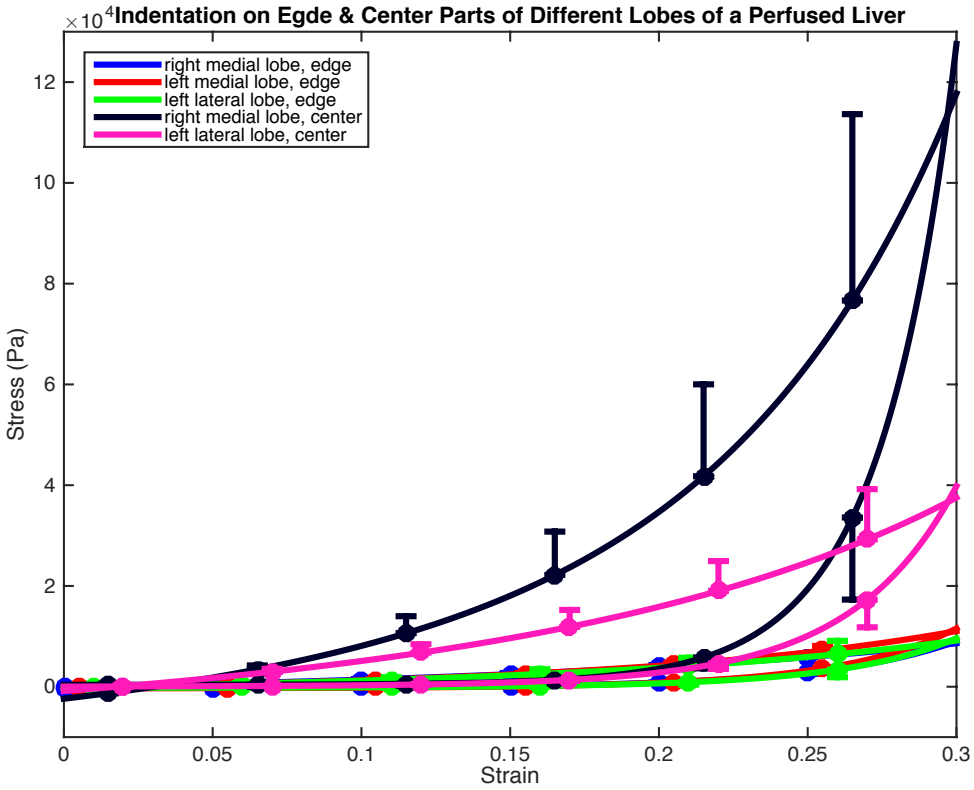


Figure 3 Hysteretic stress-strain curves of indentation tests at different parts of different lobes of a perfused porcine liver.

Table 1 Parameters of the Ogden model representing indentation experimental data and energy lost density of each hysteresis curve.

| | Lost Energy Density (J/m^3) | $\mu$ | $\alpha$ | $\mu\times\alpha$ | c | $R^2$ |
|---|---|---|---|---|---|---|
| Right Medial Lobe, Edge (Loading) | 4.76E+02 | 2.47E+03 | -3.12 | -7.70E+03 | -8.33E+01 | 1.0000 |
| Right Medial Lobe, Edge (Unloading) | | -31.69 | 29.87 | -9.47E+02 | -2.86E+02 | 1.0000 |
| Left Medial Lobe, Edge (Loading) | 4.97E+02 | 1.34E+03 | -5.15 | -6.88E+03 | -1.58E+02 | 1.0000 |
| Left Medial Lobe, Edge (Unloading) | | -21.96 | 33.30 | -7.31E+02 | -3.32E+02 | 1.0000 |
| Left Lateral Lobe, Edge (Loading) | 4.49E+02 | 1.56E+03 | -4.30 | -6.71E+03 | -1.39E+02 | 1.0000 |
| Left Lateral Lobe, Edge (Unloading) | | -16.03 | 34.00 | -5.45E+02 | -2.20E+02 | 1.0000 |
| Right Medial Lobe, Center (Loading) | 3.90E+03 | 6.42E+03 | -7.27 | -4.67E+04 | -2.38E+03 | 1.0000 |
| Right Medial Lobe, Center (Unloading) | | -6.94 | 53.04 | -3.68E+02 | 3.76E+02 | 1.0000 |
| Left Lateral Lobe, Center (Loading) | 1.78E+03 | 7.89E+03 | -3.82 | -3.02E+04 | -8.39E+02 | 1.0000 |
| Left Lateral Lobe, Center (Unloading) | | -33.10 | 37.77 | -1.25E+03 | 1.93E+01 | 1.0000 |

At the end of the experiment, we measured the liquid volume fraction of the porcine liver, which is required by the modeling team and is useful for developing biphasic constitutive models of liver tissue. The liquid volume fraction is the ratio of the volume of liquid and whole liver (volume of blood and solid liver tissue). We first measured the weight (910 g) of the liver w/o liquid inside when it came. Next, we used surgical clamps to block all main vessels at the end of the perfusion experiment and measured the weight (1640 g) and volume (1500 cc) of the liver w/ liquid and clamps. We loosened the clamps and drained the liquid out of the liver. Then we measured the weight (1208 g) and volume (1250 cc) of liver w/o liquid. The weight of clamps was 79 g. By using all the information mentioned above, we calculated the liquid volume fraction of our porcine liver to be about 44%. One thing to note is that we cannot let the solution inside the innumerable small vessels completely drain without damaging the cells and preventing the liquid inside cells going out. So, the value of the liquid volume fraction is only a rough number.

5. Body habitus graphical and physical modeling

During Y2, this group was integrated with the group, numerical methods for real-time modeling, working on modeling jointly.

6. Medical requirements and assessment

During Q1 of Y2, the group had nothing to report.

During Q2 of Y2, we evaluated existing perfusion models and coordinated activity with the UCLA Department of Laboratory and Animal Medicine in order to utilize discarded animal tissue immediately after sacrifice. The team was able to harvest sample porcine livers successfully along with the hilum of the liver containing individual vessels. The group has now reconfigured a perfusion pump and static pressure bags of saline with osmotic additives in order to perfuse the liver in the short term and measure its mechanical properties with the systems delineated above. We have successfully cannulated the hepatic artery and the portal veins and have an additional pump that returns the egress of the effluent back to a temperature controlled reservoir.

During Q3 of Y2, two porcine liver harvest procedures were performed. The group also finalized the ex-vivo perfusion system design and completed construction of prototype.

During Q4 of Y2, two fresh porcine livers were harvested, and elastic properties were characterized along with Dr. Candler's group. The group made a contribution to a novel manuscript on the description of liver mechanical properties.

7. Open standards development for virtual anatomic models

During Q1 of Y2, Virtual liver models are essential in simulation platforms dealing with virtual surgery and training. The complexity inherent in the liver functionality, which stems from the blood flow as well as complex liver movements render the deformations to be high in computational complexity. Integrating the comprehensive model requires a novel approach to the open standards required for the medical simulation purposes. Conventional simulation platforms that support simulations with a generic computing setup (using Central Processing Unit) needs to be accommodated.

Our focus is on the medical applications related to surgical simulations, where the greatest importance is given to (a) the accuracy of the soft tissue deformation response, (b) the real-time nature of the computations, and (c) the usage of patient-specific geometry. There are many potential applications for such models, and have been investigated for application domains such as the virtual surgery simulation. Physics-based methods, such as finite element and mass-spring, allow for a broad array of simulations, from gross posture changes to subtle day-to-day deformations like tumor regression. Mass-spring systems typically employ a linear elastic material model, providing fast, stable deformations. However, biological tissues exhibit a hyper-elastic response beyond small deformations. Finite element models can provide physiologically realistic deformations, but they can be computationally expensive and typically apply a tetrahedral meshing which may lower model resolution.

Our initial observation: We performed initial studies using SimTK, an NIH support open simulation platform, for better understanding the steps involved in such a development. We integrated a generic liver model with patient specific geometry to first study the model rendering complexity. We then integrated a C++ based in-house developed mass-spring approach for simulating the liver deformations. Our observations showed that

while the SimTK platform was able to render the liver geometry in real-time as a surface shell, rendering the entire liver volume was limited. This is because of the limitation in the platform's ability to use the graphical processing units for a better rendering. An in-house developed rendering module showed that SimTK can be improved with such a rendering capability. In addition, our deformation capability also showed that while simple displacements limited the frame rate to <2 frames per second, instabilities caused by bone and other movements rendered even the most-simplistic mass-spring approach not compatible with SimTK for real-time purposes. Future studies will focus on approaches to use GPUs for further improving the deformation frame rates.

GPU based biomechanical modeling and integration with a opensim platform

As a first step towards improving the computing time, we developed an open source mass spring GPU based approach for integrating with the simtk standards. The model mechanics were maintained to be simplistic enough to account for a generic tissue perturbation. Our analysis showed that the framerate can be improved from 2 to ~10 frames per second. The bottleneck was observed to be the interaction of the data from the CPU to the GPU.

During Q2 of Y2, Virtual liver models are essential in simulation platforms dealing with virtual surgery and training. The complexity inherent in the liver functionality, which stems from the blood flow as well as complex liver movements render the deformations to be high in computational complexity. Integrating the comprehensive model requires a novel approach to the open standards required for the medical simulation purposes. Conventional simulation platforms that support simulations with a generic computing setup (using Central Processing Unit) needs to be accommodated.

Our focus is to develop a simplistic machine learning platform that can learn liver deformations. Since the correlation between the observed voxel deformation and the YM distribution is not explicit, it can be construed that a direct correlation might not exist. To account for this, we developed a deep neural network model to transform the individual voxel deformations into the corresponding YM distributions. The deep neural network employed in this work is a fully connected seven-layer network. As inputs, we used the voxel's Hounsfield intensity, 3D location, and deformations that were calculated from the virtual liver phantom. The output of the network was the YM associated with each voxel. The number of neurons in the hidden layer were optimized for the best result, ultimately settling at 200. A simple schematic of the network is shown in figure 2(a). Annotated data was then split between a training set and a test set as 25% to 75%, respectively. As the training data was fed through the DNN, a series of weights and biases were optimized to minimize a loss function. Currently, the most widely used approach for neural network training is stochastic gradient descent (Bottou 2010). Stochastic gradient descent (SGD) trains on smaller batches of training data, called epochs. Within an epoch, the training batch is iterated through several times, randomly choosing data points to estimate the gradient. An adaptive sub-gradient method, with dynamic learning rates was employed for network training (Zeiler 2012).

The accuracy of the network was continually monitored by inferring an output from the test data, and comparing to the ground truth expectations. Figure 2(b) illustrates the flow of data for the full network architecture. The seven input values were sent through the hidden and output layers, while the known expectations (ground-truth YM values) were sent to the loss and accuracy functions. The result of the output layer was then sent to the loss function, accuracy function, and training algorithm, which updated the weights and biases of the hidden and output layers and were used to compute the network accuracy (further discussed in section 2.2.3).

Neuron activation function. The neurons of the hidden layer took the data from each neuron of the input layer, apply a matrix multiplication with weighting factors, add a bias, and then apply a non-linear activation function. These weights and biases are the values adjusted during training and allows the network to learn. Converting this to a non-linear response is important because a composition of linear functions remains a linear function, so the network abstraction is limited no matter its depth. The activation function chosen for this network was the sigmoid function (eq. 6) (Neilsen 2015). The sigmoid function is essentially a smoothed out step function that was chosen because there was no loss of data for negative values, which is typical for other activation functions, such as hyperbolic tangent and rectified linear unit function.

Loss and accuracy measures. The loss function was applied during training to calculate the error between the output of the feed-forward neural network YM inference and the ground truth YM values. Since the output of the network was intended to be a physical quantity, quadratic cost was implemented as the loss function (Kline and Berardi 2005, Neilsen 2015). The accuracy was calculated (in equation 8) as an absolute percent error between the estimated YM values and the ground truth YM values, with a target of 0.1 mm accuracy.

The accuracy reported was also averaged over the number of samples in the test data during training, and the number of samples in the independent data when inferred results with the fully trained network.

**Supervised learning using the virtual phantom:** the virtual liver phantom geometry was obtained from anonymized liver CT geometry of both a right and left liver. Each liver phantom voxel was assigned a normal ground-truth Young's modulus based upon the HU value of the source CT, with elasticity values ranging between 1 and 20 kPa—an extended approximation of the range of elastic modulus values for normal and fibrotic liver tissue (Santhanam, Min et al. 2010, Hinz 2012). This resulted in a locally heterogeneous elasticity distribution, which was further modified to represent different diseased tissue that might be seen in liver radiotherapy cases as described in section 3.2.3. The virtual liver phantom was deformed from the initial source geometry to a target geometry based on the boundary constraints derived from the 4DCT data while the displacement of each voxel of the virtual liver phantom was taken for the learning process.

During Q3 of Y2, we focused on developing a simplistic machine learning platform that can learn liver deformations. Virtual liver models are essential in simulation platforms dealing with virtual surgery and training. The complexity inherent in the liver functionality, which stems from the blood flow as well as complex liver movements render the deformations to be high in computational complexity. Integrating the comprehensive model requires a novel approach to the open standards required for the medical simulation purposes. Conventional simulation platforms that support simulations with a generic computing setup (using Central Processing Unit) needs to be accommodated.

We present a machine learning approach for estimating liver displacement measurements at a voxel- by-voxel level. Our approach employs a constrained Generalized Adversarial Neural Network (cGAN) that learns the liver tissue displacement distributions in a supervised manner. For generating the training data, we employed an inverse elasticity estimation process for a 4DCT dataset. A linear elastic biomechanical model was employed to estimate the liver tissue's displacement distribution for known deformation during a given breathing cycle as acquired by the 4DCT. The voxel-by-voxel elastic distribution was then taken as a label while the end-exhalation 4DCT geometry was taken as data for the learning process. Once trained, the cGAN generated the label (or elasticity) for given data (liver geometry) images. The estimated elasticity was then validated using (a) direct comparison with the ground truth elasticity data using an L2-norm, (b) comparison of the deformation vector fields generated using the cGAN estimated elasticity with ground truth deformation vector fields, and (c) regenerating synthetic 4DCT and comparing with the ground-truth 4DCTs using 3 image

similarity metrics: Mutual Information (MI), Structured Similarity Index (SSIM), and Normalized Cross Correlation (NCC).

Since the correlation between the observed voxel geometry and the YM distribution is not explicit, it can be construed that a direct correlation might not exist. To account for this, we developed a deep neural network model to transform the individual voxel geometry into the corresponding YM distributions. The deep neural network employed in this work was a constrained Generalized Adversarial Network [24]. This network consisted of two neural networks, Generalizer and Discriminator networks. The generalizer network was focused on generating the label images that matched the training data. The matching process was performed by the discriminator network. The adversarial nature of the two networks enabled both the networks to be developed simultaneously. As inputs, we used the voxel's Hounsfield intensity while the output of the generator network was the YM associated with each voxel.

The generalizer network consisted of a 5-layer neural network, of which the first 3 layers were convolutional neural networks and the last 2 layers were regular fully connected neural networks. As the training data were fed through the generator, each layer of the neural networks worked as follows: The neurons of the hidden layer took the data from each neuron of the input layer, applied a matrix multiplication with weighting factors, added a bias, and then applied a non-linear activation function. Converting this to a non-linear response was important because a composition of linear functions remained a linear function, so the network abstraction was limited no matter its depth. The activation function chosen for this network was the sigmoid function [25]. The sigmoid function is essentially a smoothed-out step function that was chosen because there was no loss of data for negative values, which is typical of other activation functions, such as hyperbolic tangent and rectified linear unit function. During the optimization process, the series of weights and biases associated with the generator network were optimized.

The discriminator network consisted of a 4-layer neural network of which the first 2 layers were convolutional neural networks and the last 2 layers were regular fully connected neural networks. The accuracy of the network was continually monitored by inferring an output from the discriminator. The input values for the discriminator came from the generator neural network and the ground truth labels. To compute the accuracy, the inputs were sent through the hidden and output layers. The result of the output layer was then sent to the loss function, accuracy function, and training algorithm. The loss function was applied during training to calculate the error between the output of the feed-forward neural network YM inference and the ground truth YM values. Since the output of the network was intended to be a distribution of a physical quantity, quadratic cost was implemented as the loss function [25, 26]. The weights and biases of the hidden and output layers associated with the discriminator network were updated to enable refining the discriminator network and ultimately the generator network.

Currently, the most widely used approach for neural network training is an ADAM optimizer, which is efficient in addressing large datasets. The method aims at updating the neural network weights based on the moments of the gradients. The approach is more suitable for the learning setup [27], where the gradients are sparse and invariant to re-scaling. Unlike conventional neural networks, the update for the network weights is performed for both the discriminator as well as generator deep neural networks. For scenarios where the discriminator does not effectively discriminate the generated YM values, the optimizer is performed to update the discriminator weights accordingly.

The virtual liver phantom geometry was obtained from anonymized liver CT geometry of both a right and left liver. Each liver phantom voxel was assigned a normal ground-truth Young's modulus based upon the HU value of the source CT, with elasticity values ranging between 1 and 20 kPa—an extended approximation of the

range of elastic modulus values for normal and fibrotic liver tissue (Santhanam, Min et al. 2010, Hinz 2012). This resulted in a locally heterogeneous elasticity distribution, which was further modified to represent different diseased tissue that might be seen in liver radiotherapy cases as described in section 3.2.3. The virtual liver phantom was deformed from the initial source geometry to a target geometry based on the boundary constraints derived from the 4DCT data while the displacement of each voxel of the virtual liver phantom was taken for the learning process. Plans for the next quarter
Development of a simplistic machine learning platform for enabling even a simplistic CPU based simulation platform to compute deformations in real-time.

During Q4 of Y2, we focused on code development.

**Code development for Training study***:* the lung geometry was obtained from anonymized lung 5DCT end-exhalation scans of both a right and left lung. The DVFs associated with the end-exhalation to end-inhalation CTs (generated from the 5DCTs [1] ) were computed using an in-house optical flow registration and then used as the ground-truth displacement for the inverse elasticity estimation process [2, 3]. Each lung phantom voxel was assigned an initial ground-truth Young's modulus based upon the HU value of the source CT, with elasticity values ranging between 1 and 20 kPa—an extended approximation of the range of elastic moduli values for normal and fibrotic lung tissues [4, 5]. The resulting elasticity distribution and the source geometry were assigned the label and the data for the learning process, respectively. To this end, each lung anatomy was separated into left and right lungs and was resliced into 2D axial slices at 1 mm resolution. The elasticity was also represented in the same input format. The training process iterated for a fixed number of generator and discriminator updates.

**Code development for Validation study:** three different validation approaches were investigated. In the first approach, we compared the ground-truth with the cGAN generatd elasticity using an L2-Norm difference. From a clinical perspective, a systematic validation would include not only the elasticity distribution results but also the results obtained from its clinical usage. For this purpose, we integrated the estimated elasticity distribution and the source geometry with the biomechanical model. Once integrated, the biomechanical model generated 4D lung deformations for given boundary conditions. For our validation study, we compared the deformations obtained from the integrated model with the deformation vector fields of the ground-truth 4DCT datasets. Let $d_{a,0}$ and $d_a$ refer to the ground-truth and model generated displacements of voxel $a$, respectively. A L2-norm difference was applied to quantitate the displacement differences on a voxel-by-voxel basis. The number of voxels that converged within a certain epsilon value of ground-truth was characterized as the error quantification for the GAN estimated lung elasticity distribution. It is formulated as follows:

$$c_a = \begin{cases} 1: & \left\| |d_a| - |d_{a,0}| \right\| < \epsilon \\ 0: & otherwise \end{cases} \qquad (3)$$

$$p(\epsilon) = \frac{\sum_1^n c_a}{n} \qquad (4)$$

In (3) above, $(\epsilon)$ represents the threshold for the L2-norm of the deformation vector for each voxel $a$ within the lung volume $V$, and $c_a$ represents the error for each voxel. Two different epsilon values were investigated. First, we looked at $\epsilon_1 = 1$, or the percent of voxels that converged within 1 mm of the ground-truth deformation, as the resolution of many CT images is around one cubic millimeter. Secondly, since lung deformation can vary widely between patients and breathing phases, we looked at the percent of voxels that converged within 10% of the maximum deformation, or $\epsilon_2 = 0.1 * \max_{\mathrm{a}}(|d_a|)$. The percent accuracy $p(\epsilon)$ was then tabulated by summing the $c_a$ over all $n$ voxels in lung volume $V$ using (3) and (4).

**Code development for Validation of the cGAN displacement generated 4DCT:** while the convergence criteria provided a quantitative way to assess the elasticity estimation accuracy, an additional metric was necessary to ensure the precision of the estimated elasticity. Specifically, we wanted to ensure that the cGAN generated elasticity coupled with the boundary constraints could be used to warp the end-exhalation image to closely represent the end-inhalation image. In addition, the usage of image similarity metrics could quantify the accuracy of the ground-truth data. For this purpose, three different image similarity metrics were utilized. For each of the metrics, we assumed *x* as the cGAN generated end-inhalation CT and *y* as the ground-truth end-inhalation CT.

**Mutual Information:** mutual information (MI) is a symmetric and nonnegative similarity measure of entropy between two images that takes high values for similar images. Maximization of MI indicates complete correspondence between two images. MI assumes no prior functional relationships between the images, but rather a statistical relationship that can be evaluated by analyzing the images' joint entropy [6]. Although MI is normally applied to multimodal registration, it is often commonly used for lung alignment [7].

The mutual information is computed by comparing the image entropy values (i.e. a measure of how well-structured the common histogram is) as follows:

$$MI(x,y) = H(x) + H(y) - H(x,y) \quad (5)$$

where $H(x,y)$ is the joint entropy

$$-\sum_{x,y} p_{xy}(x,y) \log p_{xy}(x,y) \quad (6)$$

and $H(x)$ and $H(y)$ are the individual entropies

$$-\sum_{x} p_x(x) \log p_x(x). \quad (7)$$

**Structural Similarity Index Metric:** the Structural Similarity Index Metric (SSIM) examines structural changes that more closely correlate with a visual evaluation rather than differences that do not contribute to perceived image quality, which is important for lung [8-10]. It is formulated as follows [11]:

$$SSIM(x,y) = \frac{(2\mu_x\mu_y + c_1)(2\sigma_{xy} + c_2)}{(\mu_x^2 + \mu_y^2 + c_1)(\sigma_x^2 + \sigma_y^2 + c_2)} \quad (8)$$

Where the terms $(\mu)$ and $(\sigma)$ represents the mean and variance of the voxel intensities in $x$ and $y$, respectively. The SSIM can vary between -1 and 1, where a score of 1 indicates perfect similarity.

**Normalized Cross Correlation:** another image similarity metric that was used to assess the results of our study was normalized cross-correlation (NCC). NCC is a simple but effective similarity measure that is invariant to brightness and contrast variations [12]. NCC is less sensitive to linear changes in amplitude of grayscale values [12], which enables us to examine for potential intensity differences caused by the estimated elasticity. Also, NCC was previously used to overcome intensity changes caused by tissue compression difference between different breathing phases [13]. Like SSIM, NCC values range from a perfect match of 1 to a completely anti-correlated match of -1. The equation for calculating the NCC is shown as

$$NCC(x,y) = C_{xy}(\hat{x},\hat{y}) = \sum_{i,j \in R} \hat{x}(i,j), \hat{y}(i,j), \quad (9)$$

where $\hat{x}$ and $\hat{y}$ are intensity normalized images (cGAN elasticity generated end-inhalation and the ground-truth end-inhalation CT).

8. Project advisory activity

During Y2, this group has no activity to report.

- **What opportunities for training and professional development has the project provided?**

Professional development and training was provided to the following individuals:

Graduate Student Researchers:

- Daniel Canuto (Mechanical and Aerospace Engineering)
- Yi-Jui Chang (Mechanical and Aerospace Engineering)
- Qi Guo (Mathematics)
- Michael Reyes (Mechanical and Aerospace Engineering)
- Ling Li (Electrical Engineering)
- Ashkan Maccabi (Bioengineering)
- Ahmad Abiri (Bioengineering)
- Tao Zhou (Computer Science)

Postdoctoral Scholars:

- Dr. Kwitae Chong (Mechanical and Aerospace Engineering)
- Dr. Chenfanfu Jiang (Mathematics, Computer Science)
- Dr. Nathan Francis (Mechanical and Aerospace Engineering)
- Dr. George Saddik (Mechanical and Aerospace Engineering)

Surgical Resident Researchers:

- Yen-Yi Juo, M.D. (Surgery)

- **How were the results disseminated to communities of interest?**

Journal paper on biomechanical organ modeling methodology published:

Hasse K, Neylon J, Santhanam A.P. *Feasibility and quantitative analysis of a biomechanical model-guided lung elastography for radiotherapy.* Journal of Biomedical Physics and Engineering (in press).

- **What do you plan to do during the next reporting period to accomplish the goals?**

1. Fluid dynamics & tissue constitutive modeling

During the next reporting period, we will conduct further testing of our time domain model of the auto-regulated vascular model, and refine and carry out further simple simulations of the cubic porous liver

specimen with our bi-phasic SPH model, including simulations of the specific mechanical tests carried out by the Candler research group.

2. Numerical methods for real-time modeling

During the next reporting period, we will continue the investigations into cutting soft tissues as well as providing training data for machine learning and deep learning simulation of soft tissues.

3. Biomechanical and graphical modeling of organs

During the next reporting period, we will further our efforts in advancing liver elasticity measurements.

4. Tissue properties measurement and validation

During the next reporting period, we plan to use another instrument (Instron 5544) to measure the full stress-strain hysteretic curves (including tensile and compression tests) of both perfused and sectioned liver samples. So, we can have a better understanding of how the liver would behave during the transition of under tension state to under compression state.

5. Body habitus graphical and physical modeling

During the next reporting period, we will continue our modeling work.

6. Medical requirements and assessment

During the next reporting period, the group will harvest fresh porcine liver needed.

7. Open standards development for virtual anatomic models

During the next reporting period, we will complete data analysis using Magnetic Resonance datasets.

8. Project advisory activity

During the next reporting period, the group will continue to consult subject matter experts as needed.

**IMPACT**:

- **What was the impact on the development of the principal discipline(s) of the project?**

Nothing to Report.

- **What was the impact on other disciplines?**

Nothing to Report.

- **What was the impact on technology transfer?**

Nothing to Report.

- **What was the impact on society beyond science and technology?**

Nothing to Report.

**CHANGES/PROBLEMS**:

- **Changes in approach and reasons for change**

Nothing to Report.

- **Actual or anticipated problems or delays and actions or plans to resolve them**

Nothing to Report.

- **Changes that had a significant impact on expenditures**

Nothing to Report.

- **Significant changes in use or care of human subjects, vertebrate animals, biohazards, and/or select agents**

Nothing to Report.

- **Significant changes in use or care of human subjects**

Nothing to Report.

- **Significant changes in use or care of vertebrate animals.**

Nothing to Report.

- **Significant changes in use of biohazards and/or select agents**

Nothing to Report.

**PRODUCTS**:

- **Publications, conference papers, and presentations**

Journal paper on biomechanical organ modeling methodology published:

Hasse K, Neylon J, Santhanam A.P. *Feasibility and quantitative analysis of a biomechanical model-guided lung elastography for radiotherapy.* Journal of Biomedical Physics and Engineering (in press).

- **Website(s) or other Internet site(s)**

Nothing to Report.

- **Technologies or techniques**

Nothing to Report.

- **Inventions, patent applications, and/or licenses**

Nothing to Report.

- **Other Products**

Nothing to Report.

**PARTICIPANTS & OTHER COLLABORATING ORGANIZATIONS**

- **What individuals have worked on the project?**

| | |
|---|---|
| Name: | Professor Jeff D. Eldredge, Ph.D. (no change) |
| Name: | Dr. Kwitae Chong, Ph.D. (no change) |
| Name: | Mr. Daniel Canuto (no change) |
| Name: | Mr. Yi-Jui Chang (no change) |
| Name: | Joseph Teran (no change) |
| Name: | Chenfanfu Jiang (no change) |
| Name: | Qi Guo (no change) |
| Name: | Anand Santhanam (no change) |
| Name: | Michael Reyes (no change) |
| Name: | Robert Candler (no change) |
| Name: | Dr. Warren Grundfest (no change) |
| Name: | Ms. Ling Li (no change) |
| Name: | Mr. Ashkan Maccabi (no change) |
| Name: | Mr. Ahmad Abiri (no change) |
| Name: | Dr. George Saddik (no change) |
| Name: | Dr. Nathan Francis (no change) |
| Name: | Demetri Terzopoulos (no change) |
| Name: | Tao Zhou (no change) |
| Name: | Peyman Benharash (no change) |
| Name: | Erik Dutson (no change) |
| Name: | Yen-Yi Juo (no change) |
| Name: | Cheryl Hein (no change) |

- **Has there been a change in the active other support of the PD/PI(s) or senior/key personnel since the last reporting period?**

Nothing to Report.

- **What other organizations were involved as partners?**

Nothing to Report.

# Virtual Tissue Modeling for Realtime Surgical and Interventional Procedure Simulation

W81XWH-15-1-0147

**PI:** Peyman Benharash, M.D. **Org:** CASIT at UCLA **Award Amount:** $3,600,000

## Study/Product Aim(s)

- Develop a general framework for creation and sharing of virtual tissue models
- Create a prototype virtual tissue simulation of the liver and associated soft tissue and fluidic physiological systems
- Develop and integrate needed mathematical models, constitutive models, and interactive graphical models as a functional system of physics-based dynamic tissue simulations capable of real-time interaction appropriate for medical training simulators
- Create virtual injury mechanisms and surgical tools for manipulation of the virtual tissue and methods developed for integrating component models into a virtual patient body habitus model
- Demonstrate system in either a video or online interactive presentation format

## Approach

We will advance in eight Focal Areas comprising a generalized framework for Virtual Tissue models.

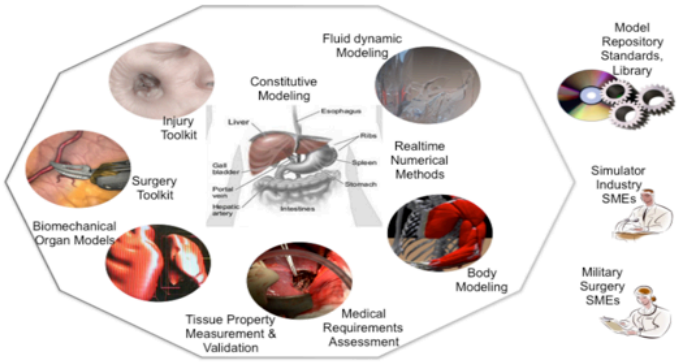


Accomplishments:
Continuation of R&D in 8 Focal Areas

## Timeline and Cost

| Activities CY | 15 | 16 | 17 | 18 |
|---|---|---|---|---|
| R&D Launch | | | | |
| Partial Integration and Demonstration | | | | |
| Full Integration and Demonstration | | | | |
| | | | | |
| **Estimated Budget ($K)** | **$600** | **$1,200** | **$1,200** | **$600** |

**Updated:** 2017-07-01

**Goals/Milestones**

**CY15 Goal** – R&D Launch
- ✓Launch 9 focal areas of R&D
- ✓Model subtype development
- ✓Tissue property data collection

**CY16 Goals** – Partial Integration and Demonstration
- ✓Partial model integration
- ✓Focal area demonstrations
- ✓Validation testing

**CY17 Goal** – Full Integration and Demonstration
- ❑Full prototype integration
- ❑Proof-of-concept demonstration
- ❑Gap analysis

**Comments/Challenges/Issues/Concerns**
- Nothing to report; project is on schedule

**Budget Expenditure to Date**

Projected Expenditure: $2,400,000
Actual Expenditure: $2,052,000